An Observational Study of Tropical Cyclone Spinup in Supertyphoon Jangmi (2008) from 24 to 27 September

NEIL T. SANGER

U. S. Air Force Weather, Barksdale Air Force Base, Louisiana

MICHAEL T. MONTGOMERY

Department of Meteorology, Naval Postgraduate School, Monterey, California

ROGER K. SMITH

Meteorological Institute, Ludwig Maximilians University of Munich, Munich, Germany

MICHAEL M. BELL

Department of Meteorology, University of Hawai'i at Mānoa, Honolulu, Hawaii

(Manuscript received 16 October 2012, in final form 31 May 2013)

ABSTRACT

An observational study of tropical cyclone intensification is performed using dropsondes, in situ flight-level data, satellite imagery, and Electra Doppler Radar (ELDORA) during the spinup of Tropical Storm Jangmi (2008) in the western North Pacific. This event was observed with research aircraft during the Tropical Cyclone Structure 2008 (TCS08) field experiment over the course of 3 days as Jangmi intensified rapidly from a tropical storm to a supertyphoon. The dropsonde analysis indicates that the peak azimuthally averaged storm-relative tangential wind speed occurs persistently within the boundary layer throughout the spinup period and suggests that significant supergradient winds are present near and just within the radius of maximum tangential winds. An examination of the ELDORA data in Tropical Storm Jangmi reveals multiple rotating updrafts near the developing eye beneath cold cloud top temperatures $\leq -65°C$. In particular, there is a 12-km-wide, upright updraft with a peak velocity of $9\,m\,s^{-1}$ with collocated strong low-level ($z < 2\,km$) convergence of $2 \times 10^{-3}\,s^{-1}$ and intense relative vorticity of $4 \times 10^{-3}\,s^{-1}$. The analysis of the corresponding infrared satellite imagery suggests that vortical updrafts are common before and during rapid intensification. The findings of this study support a recent paradigm of tropical cyclone intensification in which rotating convective clouds are important elements in the spinup process. In a system-scale view of this process, the maximum tangential wind is found within the boundary layer, where the tangential wind becomes supergradient before the air ascends into the eyewall updraft.

1. Introduction

While a 45% ($3\%\,yr^{-1}$) decrease in the 48-h track forecast error of tropical cyclones has been achieved between 1990 and 2005, only a modest decline of approximately 17% ($1.1\%\,yr^{-1}$) in the 48-h intensity forecast errors has been attained over the same period (Rogers et al. 2006). The lack of improvement in intensity forecasting may be due in part to an incomplete knowledge of the physics and dynamics of intensity change. In addition, there is no consensus on the dominant intensification mechanism. Finally, the absence of advancement in intensity forecast skill may be a result of the inherently short predictability window of tropical cyclone intensification.

The recent work of Smith et al. (2009), Bui et al. (2009), Smith and Thomsen (2010), and Smith and Montgomery (2010) has suggested that boundary layer dynamics play a more prominent role in the intensification process than thermodynamics. However, a lack of observations of boundary layer structure during intensifying storms limits our ability to evaluate this work.

To provide a context for this observational study, we review briefly three major spinup theories that have been

Corresponding author address: Lieutenant Colonel Neil T. Sanger, U.S. Air Force Global Strike Command, 245 Davis Ave. East, Suite 151, Barksdale AFB, LA 71111.
E-mail: neil.sanger@us.af.mil

DOI: 10.1175/MWR-D-12-00306.1

proposed over the past 50 years. The classical, or ''conventional'' view of tropical cyclone spinup features a deep layer of convectively induced convergence of absolute angular momentum M above the boundary layer, where the flow is assumed to be approximately frictionless so that M is materially conserved (Charney and Eliassen 1964; Ooyama 1969; Carrier 1971; Willoughby 1990).

A second hypothesis developed over the past two and half decades emphasizes thermodynamic processes and focuses in particular on a postulated positive feedback loop involving the near-surface wind speed and the evaporation of water from the underlying ocean, with the evaporation rate being a function of wind speed and thermodynamic disequilibrium (Rotunno and Emanuel 1987; Emanuel 1989, 1997, 2003; Emanuel et al. 1994; Holton 2004).

A third and recent theory described in a series of papers by Nguyen et al. (2008), Montgomery et al. (2009), Smith et al. (2009), Bui et al. (2009), and Persing et al. (2013) highlights the presence of rotating convective structures[1] and their vorticity remnants as well as their role in organizing the vorticity structure of the storm's core. These clouds collectively drive the spinup of the system-scale vortex by inducing radial inflow above the boundary layer, consistent with the previous two theories. As in the earlier hypotheses, radial convergence of M above the boundary layer in conjunction with its material conservation leads to spinup of the bulk tangential winds and an increasing radial pressure gradient there. In contrast, this new theory stresses the fact that the spinup of the maximum tangential winds actually occurs in the boundary layer below 1-km altitude.

In the boundary layer, M is reduced by the frictional torque, but the radial inflow is much stronger than above this layer due to both friction and an increase in the radial pressure gradient at the top of the layer resulting from elevated radial inflow atop the boundary layer. Spinup occurs in the boundary layer when the radial inflow is large enough to converge rings of air with radius r to small radii sufficiently rapidly so that, despite some loss of M due to friction, M/r increases. The amplification of the tangential wind by this mechanism naturally leads to the development of supergradient flow and an accompanying outward agradient force. The agradient force acts to arrest the radial inflow at the base of the eyewall, whereupon air parcels turn upward and carry their elevated tangential momentum into the eyewall. This process contributes also to the spinup of the tangential winds in the bulk vortex (Smith et al. 2009; Bui et al. 2009; Smith and Thomsen 2010; Smith and Montgomery 2010; Persing et al. 2013). The foregoing paradigms are reviewed and compared by Montgomery and Smith (2013).

The strong low-level radial inflow in the inner-core region has been documented in individual cases by Montgomery et al. (2006b), Bell and Montgomery (2008), Bell et al. (2012), and by Zhang et al. (2011) in a recent composite of dropsonde observations in mature and intensifying tropical cyclones. While these studies offer support for elements of the foregoing hypothesis, they do not demonstrate fully the chain of processes for the boundary layer spinup mechanism articulated above. Although this study displays more data analysis on boundary layer processes than in prior observational studies, it still falls short of showing the entire sequence of events associated with spinup primarily due to data limitations.

Two complementary field experiments, The Observing System Research and Predictability Experiment (THORPEX) Pacific Asian Regional Campaign (T-PARC); and the Tropical Cyclone Structure 2008 (TCS08), conducted in the summer of 2008 in the western North Pacific used research aircraft to collect data in tropical disturbances and intensifying tropical storms. For details on the T-PARC and TCS08 field campaigns, the reader is referred to Parsons et al. (2008) and Elsberry and Harr (2008). During the experiments, two typhoons, Jangmi and Nuri, were documented in considerable detail over a period of several days as they intensified, offering an opportunity to investigate the role of the boundary layer in spinup. In addition, data obtained using the Electra Doppler Radar (ELDORA) acquired during the tropical storm stage of Jangmi provide an opportunity to document the presence of rotating convection during intensification. The present paper presents the results of such an investigation for Supertyphoon Jangmi.

The paper is organized as follows. Section 2 includes a brief description of Jangmi's history. Section 3 discusses data collection and the analysis methodology used. In section 4, we examine the intensification of Jangmi over a 3-day period and carry out an azimuthally averaged analysis to determine the height of the

[1] The term ''rotating convection'' is used in lieu of vortical hot towers (VHTs), which were first described in Hendricks et al. (2004) and later studied in Montgomery et al. (2006a) and Nguyen et al. (2008), among others. To avoid any potential controversy that surrounds the definition of VHTs, the term ''rotating convection'' will be used throughout the rest of this paper. Usage of the term VHT has given some the impression that only deep convection (>12-km cloud depth) has strong rotation. However, a recent study by Wissmeier and Smith (2011) showed that even moderate convection (6–12-km depth) in a background rotation rate typical of the undisturbed tropical atmosphere can have a comparable impact on the stretching of low-level relative vorticity in comparison to intense deep convection. Thus, a broad definition is required for studying the aggregate impact of these convective elements on tropical cyclone spinup.

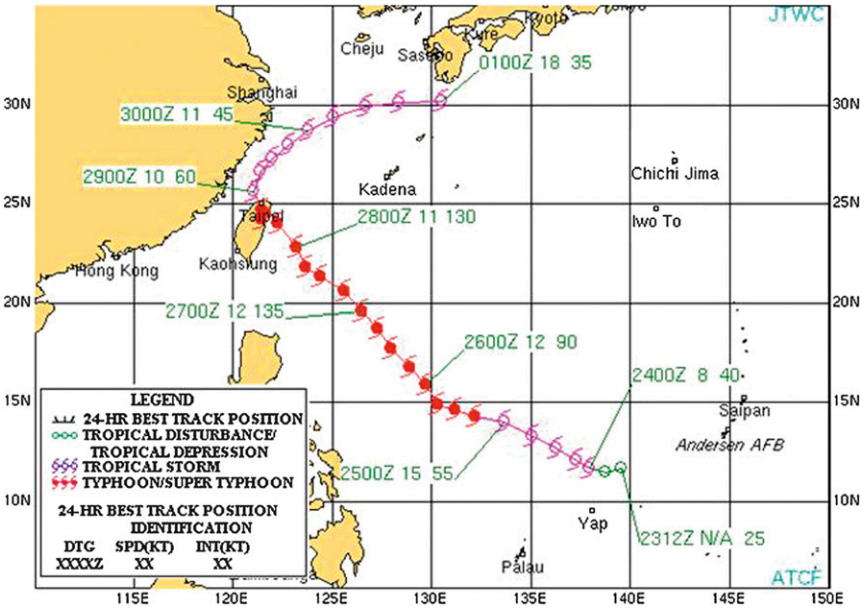

FIG. 1. JTWC best track of Supertyphoon Jangmi from Cooper and Falvey (2009). Green circle indicates a tropical depression, open purple tropical cyclone symbol is a tropical storm, and closed red tropical cyclone symbol is a typhoon. Text indicates date–time group (DDHH), storm speed (kt; 1 kt = 0.5144 m s^{-1}), and storm intensity (kt).

peak tangential wind. We use this analysis also to quantify the departure of gradient wind balance in the inner-core boundary layer region of the developing vortex. Section 5 presents analyses of the ELDORA radar observations during the spinup of Tropical Storm (TS) Jangmi in conjunction with high-resolution satellite imagery. Finally, section 6 presents a summary and conclusions drawn from the results.

2. Storm history

Supertyphoon Jangmi developed from a westward-propagating disturbance that crossed over the western North Pacific Ocean near longitude 170°E on 17 September 2008. After struggling to develop for nearly a week, the storm organized quickly and was declared a tropical depression at 1200 UTC 23 September, when it was located approximately 435 km south-southwest of Guam (Chu et al. 2009). The tropical depression evolved rapidly into a tropical storm just 12 h later at 0000 UTC 24 September as it moved on a primarily northwestward track along the periphery of the low- to midlevel subtropical ridge to its northeast. The Joint Typhoon Warning Center (JTWC) best track is shown in Fig. 1.

Jangmi continued to intensify steadily with upper-level divergence over its center and strong poleward outflow inferred from the satellite imagery (not shown). During the third penetration of the storm by the WC-130J aircraft at 2359 UTC 24 September, the radar imagery (not shown) indicated that the eye diameter decreased from around 111 to 59 km in just over 2 h (Sanger 2008a). Six hours later, at 0600 UTC 25 September, the storm was declared a typhoon with 1-min-average sustained surface wind speeds of 33 m s^{-1} and a minimum central pressure of 974 hPa (Chu et al. 2009). Over the next 18 h, Jangmi began to exhibit rapid intensification [15 m s^{-1} increase in surface wind speed within the 24-h period as defined by Kaplan and DeMaria (2003)] and reached an intensity of 46 m s^{-1} by 0000 UTC 26 September, which is shown in the JTWC best-track intensity (Fig. 2).

Subsequently, Jangmi continued a long trend of intensifying rapidly and was declared a supertyphoon at 0000 UTC 27 September with an intensity of 69 m s^{-1}. A U.S. Air Force Reserve (USAFR) WC-130J reconnaissance aircraft flying at approximately 3 km above the ocean surface measured maximum flight-level winds of 84 m s^{-1} at 0616 UTC 27 September. In addition, a dropsonde near the center of the storm indicated a surface pressure of 905 hPa at 0924 UTC and a peak surface wind speed of 71 m s^{-1} at 0751 UTC (Sanger 2008b). According to the JTWC best-track data, Supertyphoon Jangmi reached its peak intensity of 72 m s^{-1} at 0600 UTC 27 September approximately 790 km southeast of Taipei, Taiwan.

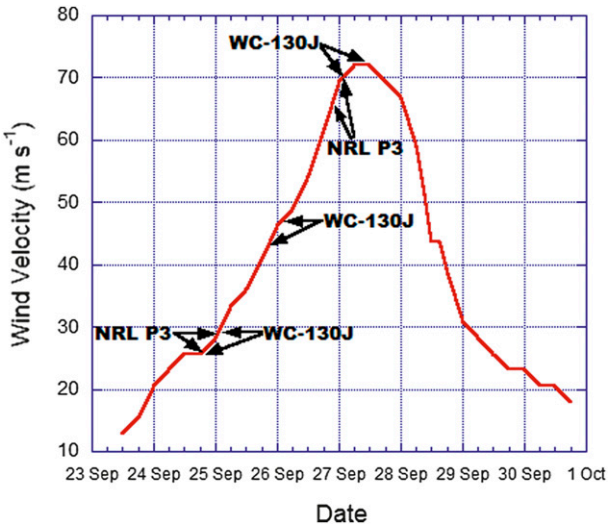

FIG. 2. JTWC best-track intensity ($m\,s^{-1}$) for Supertyphoon Jangmi from 23 to 30 Sep 2008. Arrows indicate start and stop times of the various research missions within the storm environment.

3. Data and analysis methodology

Together, the USAFR WC-130J and a Naval Research Laboratory (NRL) P-3 flew a total of six research missions into Jangmi from the tropical depression to the supertyphoon stage (Fig. 2). The NRL P-3 aircraft collected high-resolution ELDORA data in the storm while it was a weak tropical depression, a tropical storm, and a mature category-5 tropical cyclone. Since this research is focused on inner-core tropical cyclone spinup, we will discuss primarily the in situ and ELDORA data collected during intensification from the tropical storm to supertyphoon stage.

a. GPS dropsondes

The primary observational tool used in this study is the National Center for Atmospheric Research (NCAR) global positioning system (GPS) dropwindsonde (hereafter dropsonde or sonde) produced by Väisälä. The GPS dropsonde measures pressure, temperature, relative humidity (PTH), and horizontal wind speed at 2-Hz temporal resolution ($0.5\,s^{-1}$) along a Lagrangian trajectory while descending at a rate between 12 and $15\,m\,s^{-1}$ in the lower troposphere. The fall speed of the dropsonde results in a vertical resolution of around 5 m. The average PTH errors are less than 1.0 hPa, 0.2°C, and 5%, respectively, and wind errors are less than $0.5\,m\,s^{-1}$. The reader is referred to Hock and Franklin (1999) and Franklin et al. (2003) for more information on the GPS dropsonde.

Quality control of the entire set of dropsondes was performed by the NCAR/Earth Observing Laboratory (NCAR/EOL). In addition, a manual investigation of each sounding was made to eliminate any bad data points that were missed by the quality control software. Only four erroneous temperature data spikes were discovered from among the 38 eye and eyewall dropsondes released in Jangmi, and these were removed from the analysis. There were 104 dropsondes deployed and used in this study (as shown in Table 1); however, most of the dropsonde analysis presented herein focuses on the 27 eyewall soundings.

TABLE 1. Number of dropsondes launched in various regions during the three phases of Jangmi [tropical storm (TS), typhoon (TY), supertyphoon (STY)]. The total number of dropsondes for each phase is shown in far right-hand column.

Phase	Eye	Outer eye	Eyewall	Outer core	Ambient	Total
TS	3	1	11	27	5	47
TY	2	0	7	12	2	23
STY	4	1	9	18	2	34

b. In situ flight-level data

The USAFR 53rd Weather Reconnaissance Squadron (i.e., ''Hurricane Hunters'') aircrews provided the High-Density/High-Accuracy (HD/HA) flight-level data that includes geopotential height, extrapolated sea level pressure (SLP), air temperature, dewpoint temperature, wind direction, wind speed, and the peak 10-s average surface wind speed from the Stepped Frequency Microwave Radiometer (SFMR). The WC-130J was flown at an altitude between 2500 and 3000 m MSL while inside the storm. The High-Density Observation (HDOB) message transmits 30-s averages of the HD/HA data from the WC-130J aircraft, with the exception of the peak value data mentioned above (Williamson et al. 2009, their chapter 5). For more information on the SFMR data, the reader is referred to Uhlhorn et al. (2007).

The NRL P-3 1-s flight-level data were provided by NCAR/EOL and included air temperature, dewpoint, wind direction, wind speed, and geopotential height. The P-3 was flown at an altitude of approximately 4000 m MSL while inside the storm. NCAR/EOL carried out the quality control of the P-3 flight-level data. The temporal resolution of the NRL P-3 1-s flight-level data was not reduced to the coarser temporal resolution of the 30-s HDOB data from the WC-130J.

c. Storm center determination

To investigate the inner-core structure of Jangmi, we converted the in situ data from Cartesian to cylindrical coordinates in a storm-relative reference frame. Accurate center estimates to within 5 km are required for an appropriate coordinate transformation. The WC-130J aircraft center fixes were used to create a storm track

file. The JTWC best-track centers were used to ensure a reasonable starting point for the cubic spline interpolation to the first aircraft center fix. The storm centers and storm motion data were fit using a cubic spline interpolation method, and then linearly interpolated to a 10-min storm track file. Using a simple linear interpolation, this track file was then used to determine the storm-relative position and storm-relative wind for each observation point along the flight track and dropsonde descent.

The aircraft center fixes have an estimated accuracy to within one-half of the diameter of light and variable winds in the center (Williamson et al. 2009, 5–11). The mean accuracy of the centers for the tropical storm, typhoon, and supertyphoon during the individual missions were approximately 7, 5, and 3 km, respectively. Thus, the storm centers for TS Jangmi may not have been accurate enough for an appropriate transformation into storm-relative coordinates. To ensure the inherent center errors did not significantly affect the results, a sensitivity analysis of the errors on the radial and tangential winds was carried out for radii between 0 and 800 km (see Sanger 2011, chapter 3, section E). The results of the analysis indicated mean RMSE values of $\sim 2\,\mathrm{m\,s^{-1}}$ for both the radial and tangential wind speeds obtained from the dropsonde data with storm center errors less than or equal to 5 km.

To mitigate any significant errors in the analysis of TS Jangmi due to inaccurate center fixes (>5 km), we used the Willoughby and Chelmow (1982) storm centers that were made available by the National Oceanic and Atmospheric Administration/Hurricane Research Division (NOAA/HRD). These fixes, which typically have an accuracy to within ~3 km, were used to create a storm track file as detailed above.

d. Compositing technique

A simple compositing technique with bins based on storm-relative dropsonde location was used to develop the azimuthal mean of various kinematic and thermodynamical variables. Each observation point in the dropsonde and flight-level data was identified according to its radius from the storm center and placed into one of the following bins: eye, outer eye, eyewall, outer core, and ambient. These bins were estimated using the RMW, radius of the eye, and the radius of gales (total wind speed $>17\,\mathrm{m\,s^{-1}}$). The RMW was determined roughly by using the dropsonde data near the altitude of the azimuthally averaged peak tangential wind speed, or in the case of the tropical storm phase, the SFMR winds. The eye bin was defined using satellite and aircraft radar imagery and dropsonde data. The eye bin consisted of an area near the center of the storm, as observed via radar and satellite, to a radius at which the tangential wind speed remains $\leq 10\,\mathrm{m\,s^{-1}}$. The outer-eye bin was taken to cover the region of the eye immediately adjacent to the eyewall with tangential wind speeds $>10\,\mathrm{m\,s^{-1}}$. The eyewall region contained deep convection as observed on satellite and radar imagery with tangential winds at least 80% of the RMW value. In the case of TS Jangmi, the eyewall bin was taken to span a radius from 45 to 120 km. The outer-core bin was taken to be the region covering twice the RMW out to the radius of gales. The ambient region (e.g., environment) was defined approximately as the radius just beyond the outer-core region of gales to approximately 800 km.

For each of the bins, the storm-relative tangential and radial velocities were calculated. In addition, the potential temperature θ and virtual potential temperature θ_v were computed. The dropsonde data were linearly interpolated to a 50-m vertical grid from the surface to an altitude of 2000 m above the surface. The vertical grid was created using an Interactive Data Language (IDL) computer software interpolation function to fill in for missing data in the compositing and did not extrapolate beyond where the data record ends.

e. Gradient wind

Dropsonde observations and HDOB flight-level data were used to obtain an estimate of the azimuthally averaged pressure gradient for the calculation of the gradient wind curves during Jangmi's spinup using the following method. First, the gradient wind equation, from Holton (2004, p. 61), was used to solve for the gradient wind speed at each dropsonde and HDOB grid point for a fixed altitude (since the radial inflow is found to be a very small fraction of the total wind speed near the height of the maximum wind, we neglect the radial wind in all of the gradient wind estimates presented here). The air density was computed explicitly for each dropsonde and HDOB observation using the ideal gas law. For the HDOB data points, density was estimated using an average value based on dropsondes. As in Bell and Montgomery (2008), moisture was not taken into account in the density calculation, which introduces a negligible error into the gradient wind equation. Second, to facilitate the calculation of the pressure gradient at a fixed altitude, six levels were chosen for the gradient wind analysis: 275, 500, 750, 1000, 1250, and 1500 m. Then, a third-order polynomial curve fit of pressure with radius was made using the dropsonde observations as in Bell and Montgomery (2008). Next, the radial pressure gradient, $\partial p/\partial r$, was computed in units of pascals per meter ($\mathrm{Pa\,m^{-1}}$) using the raw polynomial curve fit of radius and pressure. Finally, the gradient wind curve was computed at each altitude and placed on a radial plot for comparison with the tangential wind speed measured by the dropsondes.

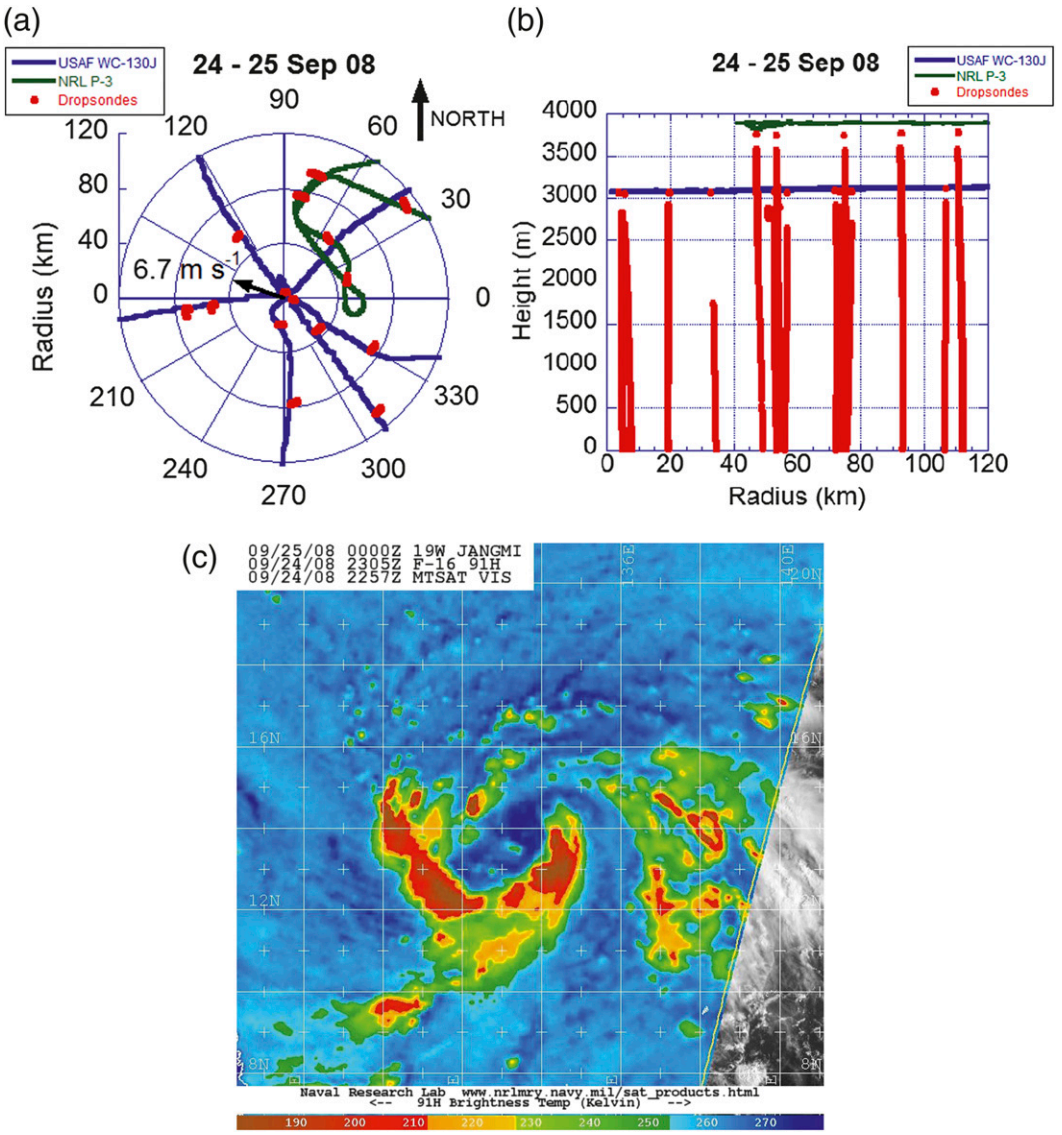

FIG. 3. Dropsonde locations, trajectories, and aircraft flight tracks in TS Jangmi from 1927 UTC 24 Sep to 0019 UTC 25 Sep 2008. Storm-relative data distributions in geographical (a) radius–azimuth (R–θ) coordinates and (b) radius–height (R–Z) coordinates. The plots display the WC-130J track (blue), the NRL P-3 track (green), and dropsonde trajectories (red). Dropsondes move cyclonically in (a). The thin black arrow in the center of (a) is the storm motion vector, with storm translation speed indicated in light black ($m\,s^{-1}$). (c) Microwave satellite imagery at 2305 UTC 24 Sep is shown to provide context of storm structure during this stage. (Imagery courtesy of Naval Research Laboratory, Monterey, CA.)

f. Satellite and ELDORA radar data

High-resolution infrared, visible, and microwave satellite imagery were used to determine the temperature and extent of cold cloud tops. They were used also to estimate the maximum extent of updrafts in TS Jangmi that were observed in the ELDORA mesoscale analyses of cells underneath cold cloud-top temperatures (≤ -65°C). In addition, these data provide a foundation for a qualitative argument that cold cloud tops associated with convective bursts are likely an indication that the convection below is rotating throughout intensification of the storm.

The NRL P-3 ELDORA data collected on 24 September were analyzed during the tropical storm stage of Jangmi to diagnose the structure of relative vertical vorticity, convergence, and vertical velocity underneath convective cells with cold cloud-top temperatures and to determine if rotation was present in the lower troposphere as suggested in modeling studies. The reader

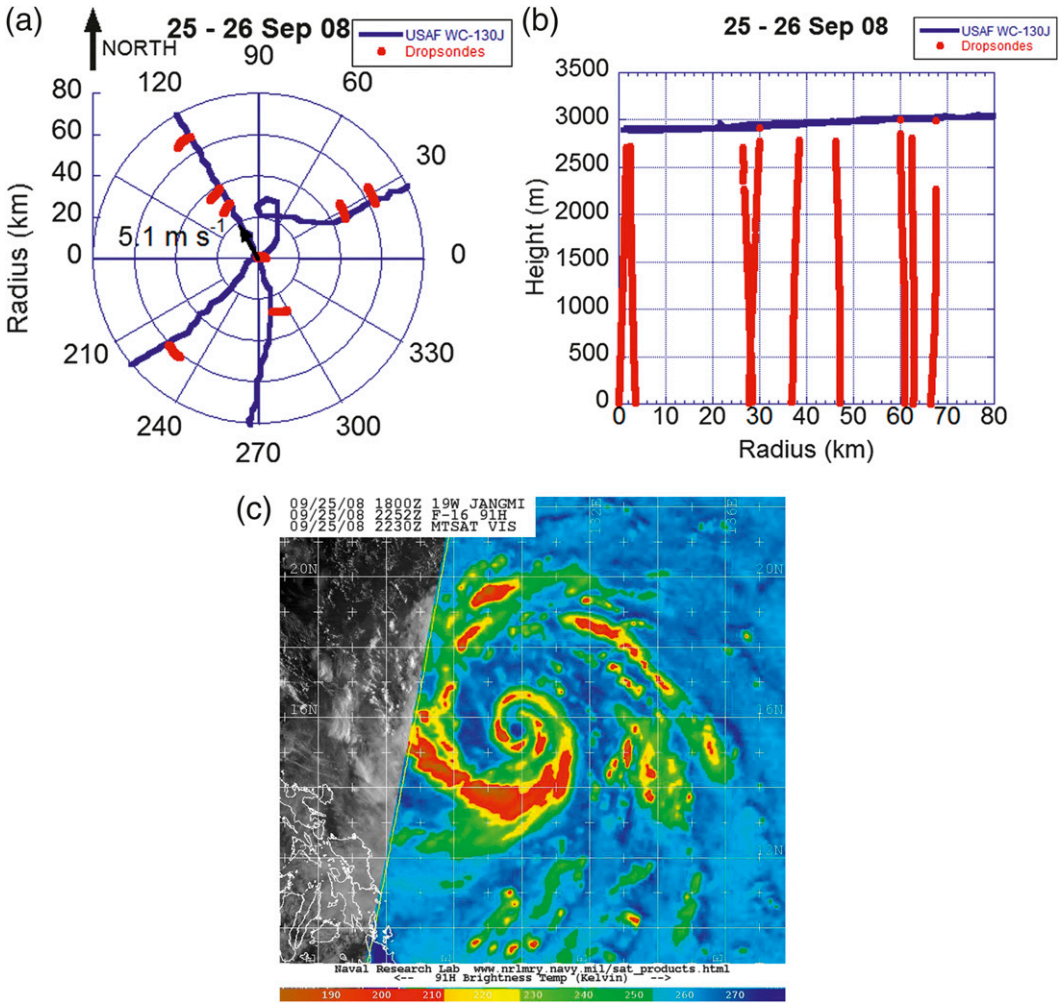

FIG. 4. Dropsonde locations, trajectories, and aircraft flight tracks in Typhoon Jangmi from 2333 UTC 25 Sep to 0113 UTC 26 Sep 2008. Storm-relative data distributions in geographical (a) radius–azimuth (R–θ) coordinates and (b) radius–height (R–Z) coordinates. The plots display the WC-130J track (blue) and dropsonde trajectories (red). Dropsondes move cyclonically in (a). The thin black arrow in the center of (a) is the storm motion vector, with storm translation speed indicated in light black ($m\,s^{-1}$). (c) Microwave satellite imagery at 2252 UTC 25 Sep is shown to provide context of storm structure during this stage. (Imagery courtesy of Naval Research Laboratory, Monterey, CA.)

is referred to Hildebrand et al. (1996, their Fig. 2) and Testud et al. (1995) for more detailed information on the ELDORA radar.

4. An azimuthally averaged view of Jangmi's spinup

The 3-day evolution of the azimuthally averaged, inner-core structure of Jangmi in the radial and vertical plane is examined utilizing in situ high-density flight-level observations and 38 eye and eyewall dropsondes released during all three stages of the storm. The number of dropsondes launched in each region of the storm for each phase of Jangmi is depicted in Table 1. The dropsondes were deployed from a USAFR WC-130J flying at an altitude of approximately 3 km and an NRL P-3 flying at around 4-km altitude. The dropsonde paths and multiple aircraft radial penetrations into Jangmi as a tropical storm, typhoon, and supertyphoon are shown in Figs. 3a, 4a, and 5a. The radial and vertical coverage of the dropsonde data points are shown in Figs. 3b, 4b, and 5b. Microwave satellite imagery in Figs. 3c, 4c, and 5c is shown to provide the context of storm structure for each of the three stages.

a. Characteristics of the low-level wind field

The near-surface locations of the Jangmi eyewall dropsondes are shown in Figs. 6a,c,e and the storm-relative

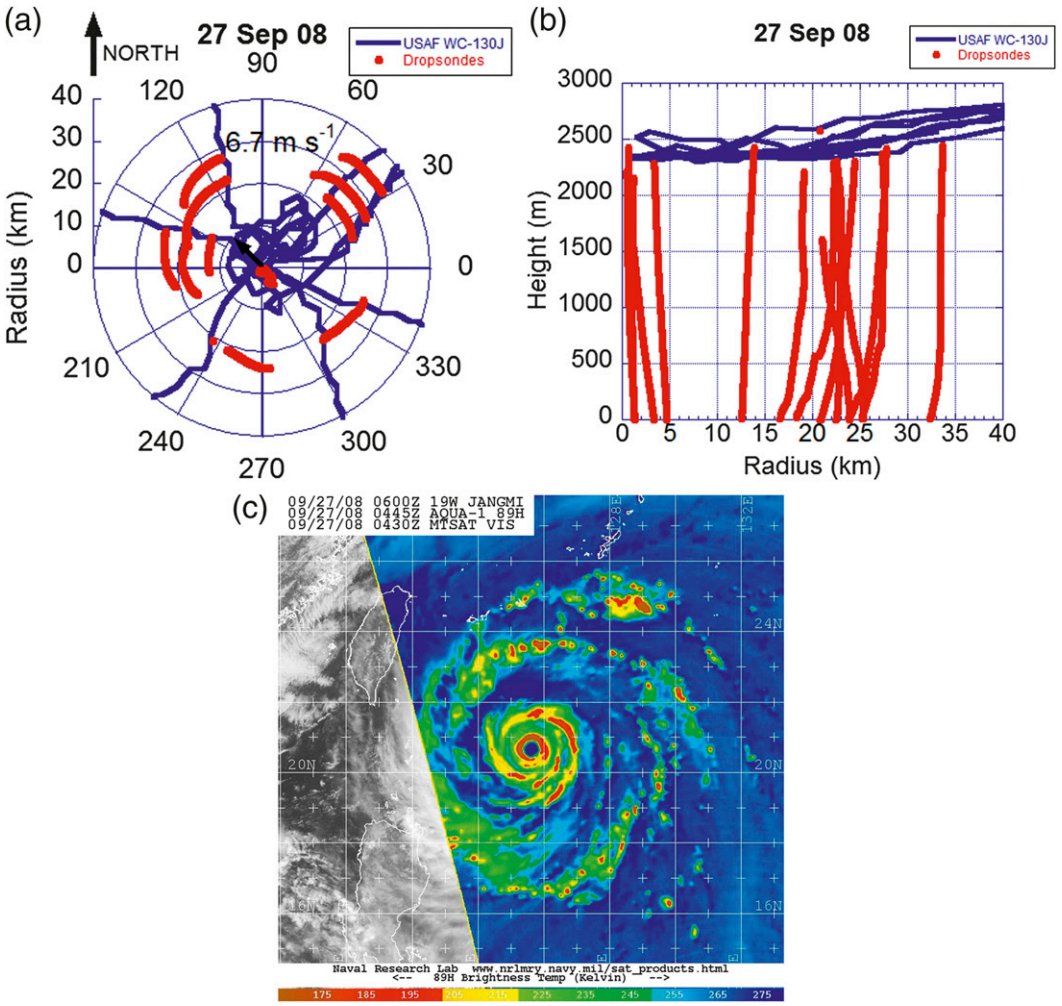

FIG. 5. Dropsonde locations, trajectories, and aircraft flight tracks in Supertyphoon Jangmi from 0615 to 0957 UTC 27 Sep 2008. Storm-relative data distributions in geographical (a) radius–azimuth (R–θ) coordinates and (b) radius–height (R–Z) coordinates. The plots display the WC-130J track (blue) and dropsonde trajectories (red). Dropsondes move cyclonically in (a). The thin black arrow in the center of (a) is the storm motion vector, with storm translation speed indicated in light black (m s^{-1}). (c) Microwave satellite imagery at 0445 UTC 27 Sep is shown to provide context of storm structure during this stage. (Imagery courtesy of Naval Research Laboratory, Monterey, CA.)

tangential wind speeds for all three stages of the storm are displayed in Figs. 6b,d,f. The red squares in Figs. 6a,c,e depict significant supergradient tangential winds (shown later in Figs. 11b,d,e). The altitudes of the plotted tangential winds are at the estimated height of the maximum tangential wind speed in the eyewall on each day.

The evolution of the tangential wind speed shown in Figs. 6b,d,f reveals that the RMW becomes distinct and closer to the storm center. Based on Figs. 6d,f, the RMW is estimated to be 55 km for Typhoon Jangmi and 24 km for Supertyphoon Jangmi. As a result of the asymmetric wind field and the small number of observations in TS Jangmi, we use the HDOB SFMR wind data to obtain a more accurate estimate of the RMW at both flight level and the surface.

The SFMR total wind observations and flight level winds retrieved from the HDOB 30-s data were used to estimate the RMW in each quadrant of TS Jangmi (see Table 2). A cubic polynomial curve was fit to all of the data points to estimate the axisymmetric mean RMW and is shown by the solid blue curve in Fig. 6b. The RMW average at flight level was ~100 km (not shown) and the SFMR RMW was ~75 km.

b. *Individual eyewall dropsondes*

Since the kinematic composites of the eyewall region (shown later in Fig. 10) are based on 27 dropsondes, it is

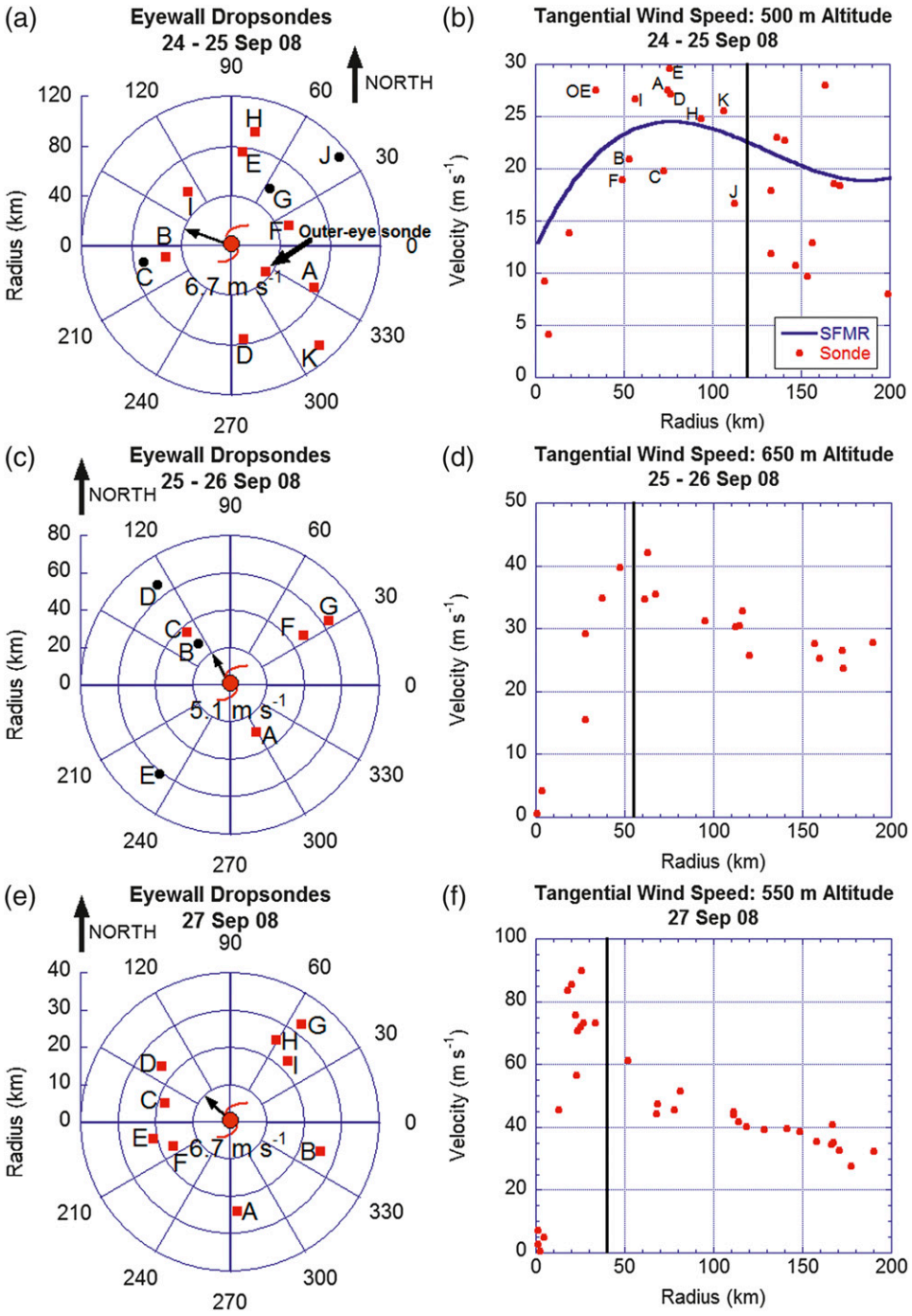

FIG. 6. (a) Near-surface radius vs azimuth displays of *only eyewall dropsondes* in geographic-oriented coordinates; dropsondes listed in order (A–K) for (a) TS Jangmi, (c) TY Jangmi, and (e) STY Jangmi. (b) Storm-relative tangential wind ($m\,s^{-1}$) from dropsonde observations vs radius out to 200-km radius at an altitude of ~500 m for TS Jangmi (red dots) and SFMR total wind speed in $m\,s^{-1}$ (solid blue curve) estimated by a third-degree polynomial curve fit of the dropsonde observations in all quadrants from 1913 UTC 24 Sep to 0032 UTC 25 Sep 2008. (d) As in (b), but without SFMR curve, at ~650-m altitude out to 200 km for TY Jangmi. (f) As in (d), but at ~550-m altitude out to 200 km for STY Jangmi. Thin, black arrow depicts storm motion vector with storm translation speed indicated in light black text near the storm translation vector ($m\,s^{-1}$). Vertical black line delineates the start of the inner-core region of the storm. Red squares in (a),(c),(e) show significant super-gradient tangential winds shown later in Figs. 11b,d,f. Dropsonde "G" is not shown in (b) since no winds were recorded at the exact height of 500 m. The SFMR curve in (b) shows an RMW of ~75-km radius.

TABLE 2. Radius of maximum total surface wind speed (RMW) in six quadrants based on Stepped Frequency Microwave Radiometer (SFMR) and flight-level (FL) observations listed in chronological order from the first radial leg to the last radial leg [east-southeast (ESE), west-southwest (WSW), south-southeast (SSE), northeast (NE), northwest (NW), and southeast (SE)] for TS Jangmi from 1856 UTC 24 Sep to 0048 UTC 25 Sep 2008. The SFMR data were collected along three WC-130J radial legs that were flown while penetrating the storm center. Because of storm asymmetry, a third-degree polynomial curve fit of the observations was used to identify the RMW in each quadrant.

Quadrant	Time	SFMR RMW	FL RMW
ESE	1856–1947 UTC 24 Sep	75 km	125 km
WSW	1947–2022 UTC 24 Sep	70 km	125 km
SSE	2114–2147 UTC 24 Sep	90 km	90 km
NE	2147–2257 UTC 24 Sep	65 km	100 km
NW	2258–2352 UTC 24 Sep	85 km	120 km
SE	0000–0047 UTC 25 Sep	65 km	70 km

of interest to study the individual dropsondes released in the eyewall (Figs. 7–9). A majority (18 of 27) of the radial wind profiles for these sondes during the evolution of Jangmi show a radial inflow layer from the surface to between 600- and 1000-m altitude. The peak tangential wind speed in 26 of the 27 sondes occurred *within* the boundary layer, whose depth was estimated to be at least 1250–1500 m, based on the layer of gradient wind imbalance discussed below in section 4e (and shown later in Fig. 14). Furthermore, 23 of the 28 sondes had the maximum tangential wind speed at or below an altitude of 600 m. Several profiles had peak tangential winds between 100 and 300 m above the sea surface. An inspection of the wind data above 2000 m for all 27 of the eyewall sondes revealed that only two of them contained the peak tangential wind in this region during the tropical storm and typhoon stage.

c. Kinematic composites

The azimuthal composites of tangential and radial wind for all three stages of Jangmi are shown in Fig. 10 for the eye (center of circulation out to a radius at which the tangential wind remains $\leq 10\ \mathrm{m\ s^{-1}}$), eyewall (region with deep convection and tangential winds at least 80% of the RMW value), outer core (twice the RMW out to the radius of gales), and environment (just beyond outer core to ~800-km radius) regions of the storm.

In all three stages, there is mean radial inflow from the surface to an altitude of at least 1 km in the eyewall region of the storm. The peak azimuthally averaged tangential wind speeds are observed in the eyewall at an altitude of around 500 m in TS Jangmi and Supertyphoon Jangmi and about 650 m in Typhoon Jangmi. It will be shown later (in Fig. 14) that these altitudes are well within the azimuthal-mean boundary layer of the system-scale circulation. These findings are consistent with observational results (Franklin et al. 2003; Powell et al. 2003; Montgomery et al. 2006b; Bell and Montgomery 2008; Giammanco et al. 2008), the theoretical analyses of Kepert (2001), Zhang et al. (2001), and Smith et al. (2009), and the numerical model results of Kepert and Wang (2001), which found also that the maximum wind speeds occurred at a height of around 500 m. The new intensification theory of Smith et al. (2009) discussed in section 1 provides a dynamical explanation for how the maximum tangential winds can exist in the frictional boundary layer and how strong radial inflow in this region of the storm can lead to the development of supergradient winds.

d. Gradient wind

Figures 11a,e show the cubic polynomial curve fits to the pressure data from the HDOB and dropsonde observations, while Fig. 11c depicts only the pressure curve fit based on the dropsonde measurements. The curve fits are judged to be very good with coefficient of determination values, r^2, between 0.92 and 0.98 (Figs. 11a,c,e) The dashed blue curves in Figs. 11b,d,f are the gradient wind estimates derived from the cubic polynomial fit to the dropsonde pressure data. On all three days, the tangential winds are most supergradient near and just within the RMW relative to the dropsonde-derived gradient wind curve. The dashed green curves in Figs. 11b,d,f provide an independent estimate of the axisymmetric gradient wind using the HDOB data, when they are available. The gradient wind computations using both the HDOB and dropsonde observations indicate the presence of supergradient winds near the RMW during the spinup of the storm.[2] Sanger (2011, see appendixes C–E) shows similar results at the five other altitudes analyzed. The maximum gradient wind is radially outward from the maximum supergradient wind in the tropical storm, typhoon, and supertyphoon phase of Jangmi.

The HDOB data have limitations in the eyewall region due to assumptions of a constant radial pressure gradient from flight level to the surface and hydrostatic balance in a region of significant upward and downward vertical velocities. However, plots of radial pressure profiles of the HDOB and dropsonde data at the surface and 500-m altitude (Figs. 12a,b) suggest that these

[2] For TS Jangmi, the WC-130J radar imagery revealed that only two supergradient wind observations may have been influenced by deep convection. These radar observations disprove the null hypothesis that the supergradient winds were merely convective wind gusts. However, just because a supergradient wind observation is near an area of convection does not necessarily mean it is a result of the convection. Instead, it may be the result of boundary layer dynamics.

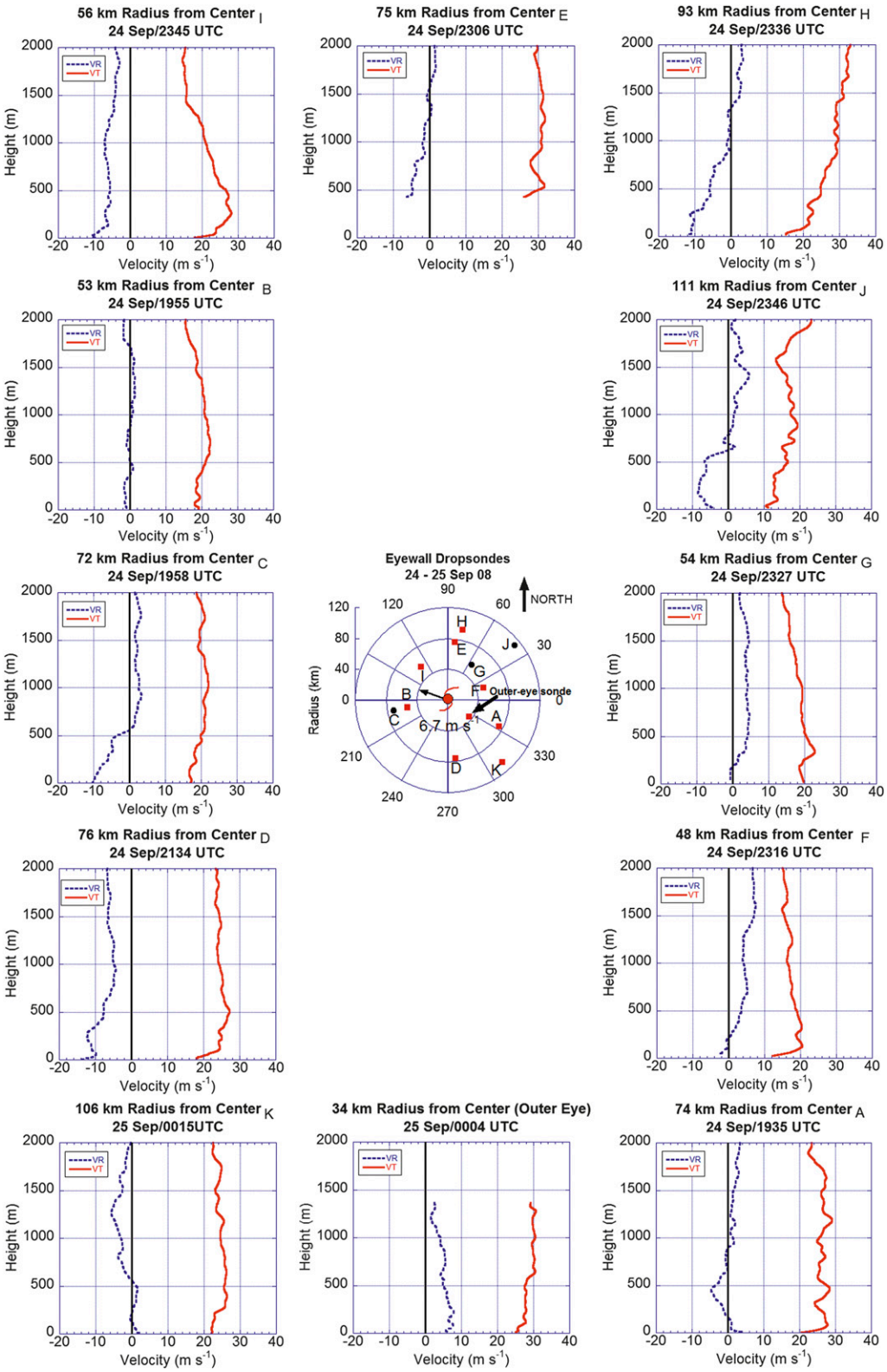

FIG. 7. TS Jangmi tangential wind (solid red line) and radial wind (dotted blue line) profiles ($m\,s^{-1}$) for eyewall sondes from 24 to 25 Sep 2008. Dropsonde locations shown in geographic-oriented R–θ plot in middle labeled with letters (A–K) according to order of launch placed relative to the storm center and solid red squares indicate supergradient winds. The dropsonde altitudes are all at or near the surface.

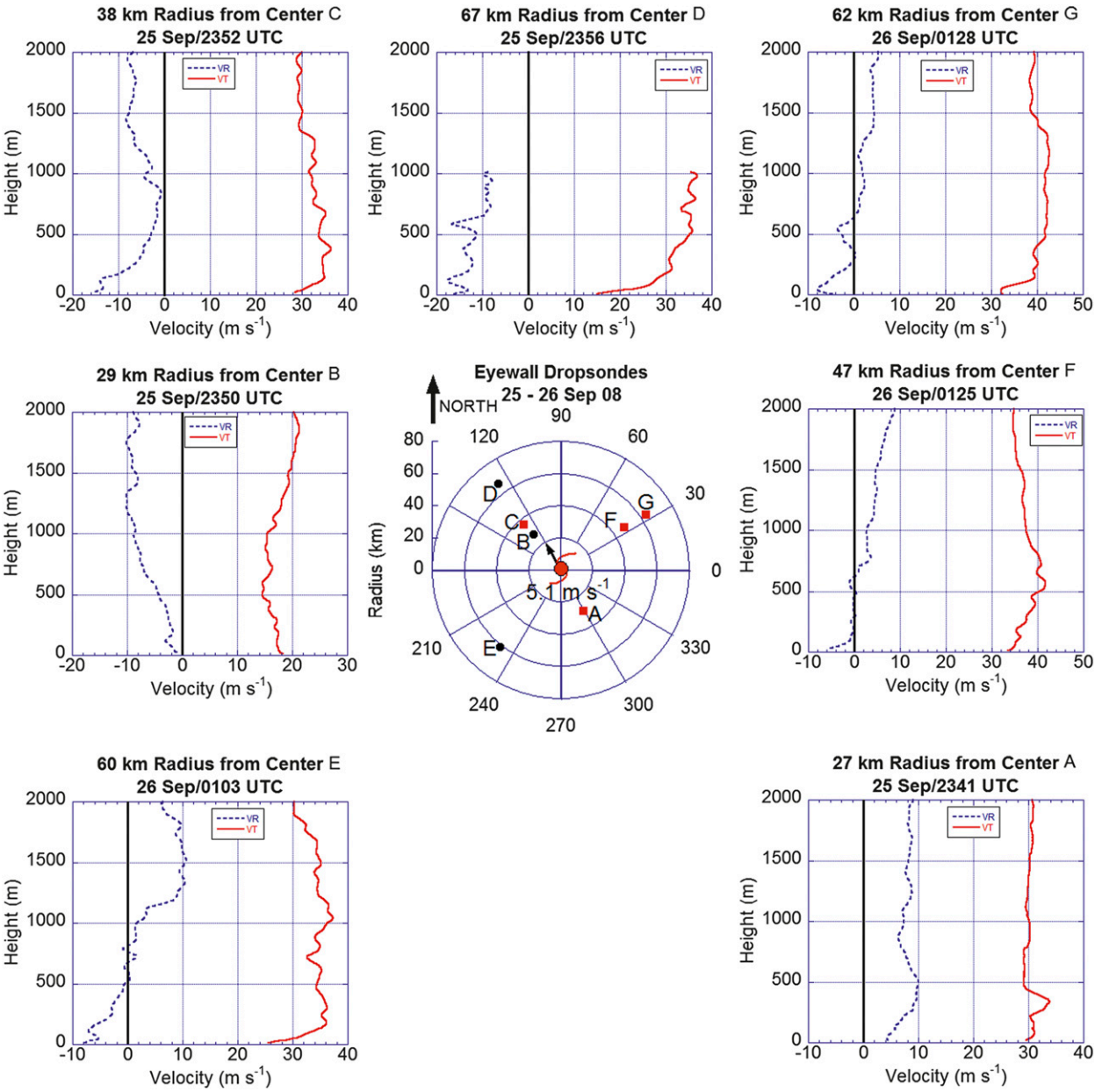

FIG. 8. Typhoon Jangmi tangential wind (solid red line) and radial wind (dotted blue line) profiles ($m\,s^{-1}$) for all eyewall dropwindsondes from 25 to 26 Sep 2008. Dropsonde locations shown in geographic-oriented R–θ plot in middle of page are labeled with letters (A–G) according to order of launch and placed in approximate location relative to the storm center and solid red squares indicate supergradient winds. The dropsonde altitudes are all at or near the surface.

limitations were not significant. It is clear from Figs. 12a,b that, for the TS stage, there is only a small discrepancy between the HDOB-derived and dropsonde-derived radial pressure profile in the boundary layer beneath the eyewall region. Thus, for TS Jangmi, it is reasonable to use the HDOB extrapolated SLP as a proxy of the azimuthally averaged pressure field to calculate the gradient wind speed. However, the asymmetric structure of TS Jangmi poses some concerns of using an axisymmetric gradient wind during this stage.

The significantly increased scatter of the pressure data and the reduced r^2 values found in Fig. 11a raises a question about the representativeness of the axisymmetric gradient wind during the tropical storm stage of Jangmi due to the large degree of convective asymmetry apparent in satellite (Fig. 3c) and radar observations (not shown). The cubic

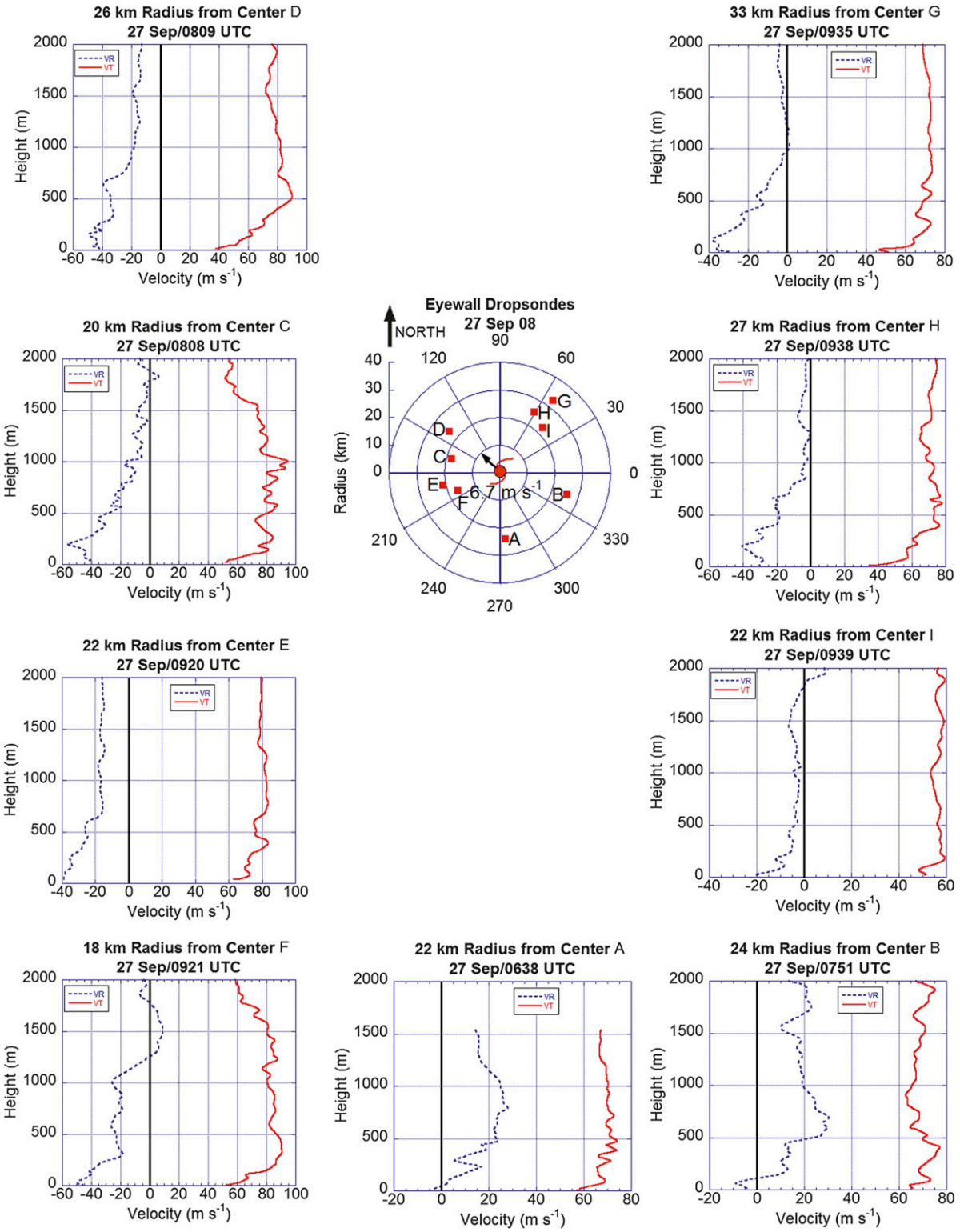

FIG. 9. Supertyphoon Jangmi tangential wind (solid red line) and radial wind (dotted blue line) profiles in $m\,s^{-1}$ for all eyewall dropwindsondes on 27 Sep 2008. Dropsonde locations shown in geographic-oriented R–θ plot in middle of page are labeled with letters (A–I) according to order of launch and placed in approximate location relative to the storm center and solid red squares indicate supergradient winds. The dropsonde altitudes are all at or near the surface.

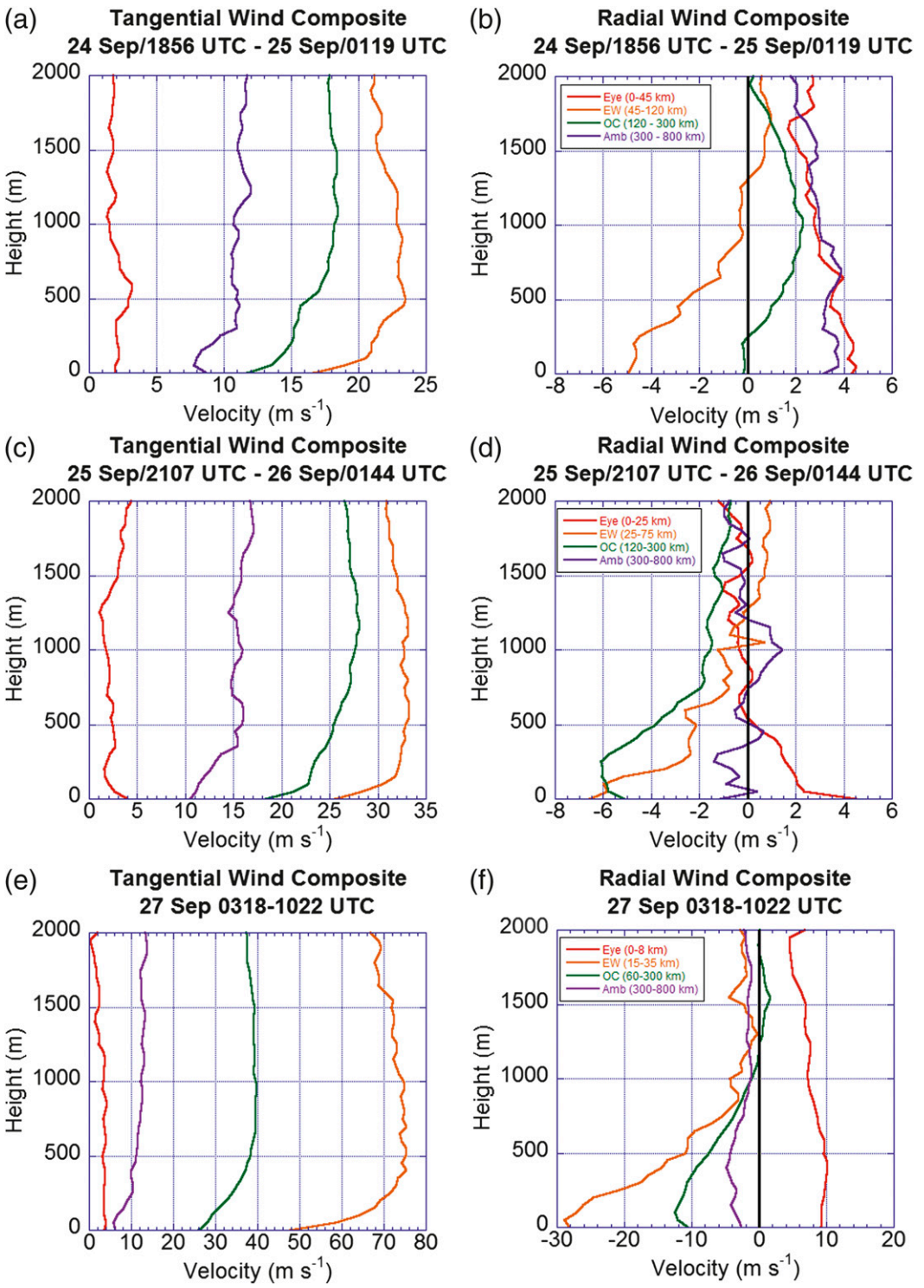

FIG. 10. Low-level (0–2 km) (left) tangential wind speed ($m\,s^{-1}$) and (right) radial wind speed ($m\,s^{-1}$) composite soundings for (a),(b) TS Jangmi; (c),(d) TY Jangmi; and (e),(f) STY Jangmi in the eye (red line), eyewall (EW; orange line), outer core (OC; green line), and ambient (Amb; purple line) regions of storm.

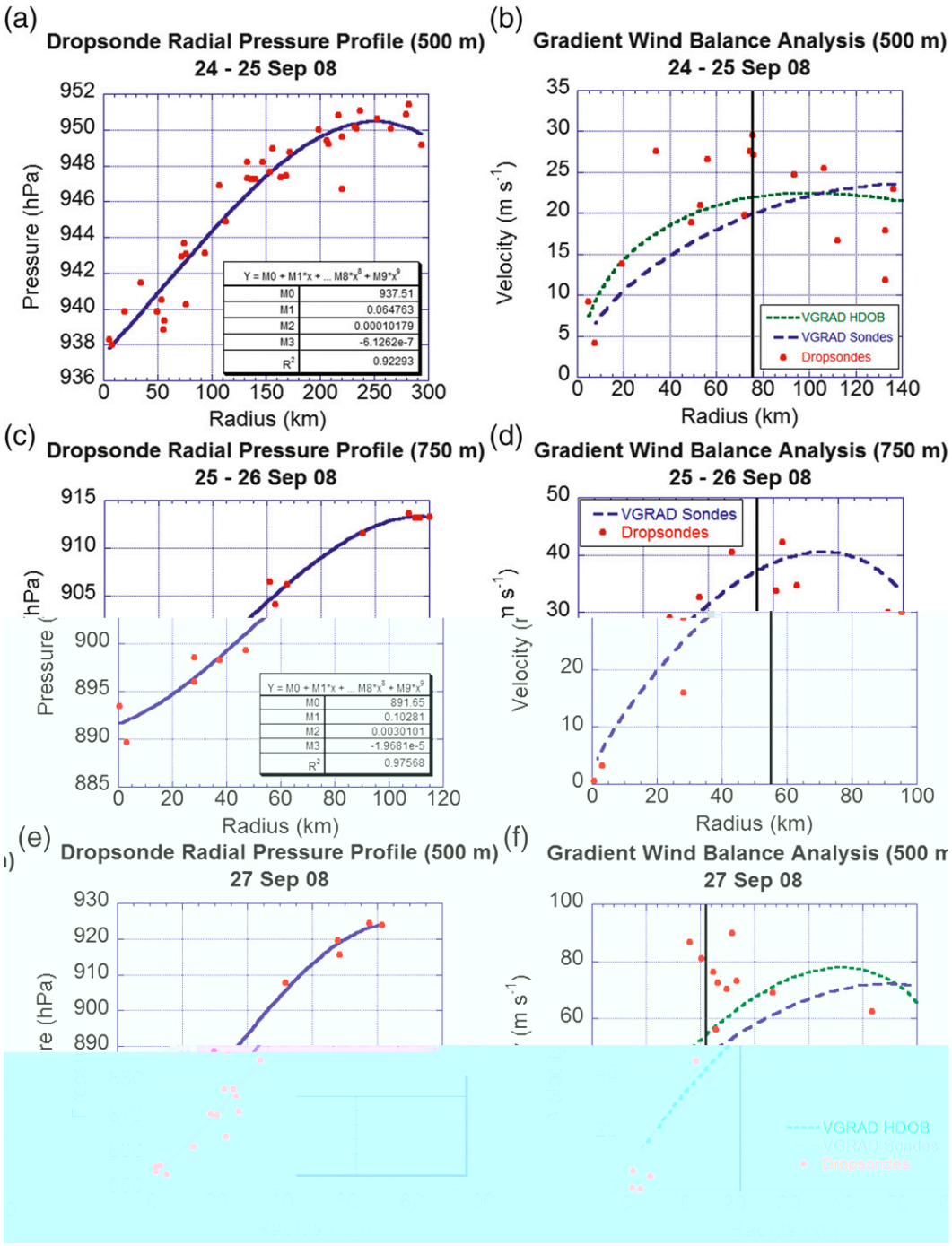

FIG. 11. Observed pressure (hPa) from dropsondes (solid red circles) and third-degree polynomial fit (solid blue line) at (a) 500 m for TS Jangmi, (c) 750 m for Typhoon Jangmi, and (e) 500 m for Supertyphoon Jangmi. Inset table shows curve fit coefficients and r^2 values. Tangential wind (m s^{-1}) at (b) 500 m for TS Jangmi, (d) 750 m for Typhoon Jangmi, and (f) 500 m for Supertyphoon Jangmi from dropsondes (solid red circles) and gradient wind from HDOB data (short-dashed green curve) and dropsonde data (long-dashed blue line). The solid black vertical lines in (b),(d),(f) denote the mean RMW.

polynomial curve fit and radial profiles in individual quadrants of the HDOB-extrapolated sea level pressure, geopotential height, and tangential wind reveal asymmetries in these fields also (Sanger 2011, Fig. 17 and Figs. 50–52).

To investigate the issue of asymmetries in TS Jangmi described above, we used the HDOB data to perform an uncertainty estimate of the gradient wind. The uncertainty estimate was conducted via a quadrant-by-quadrant

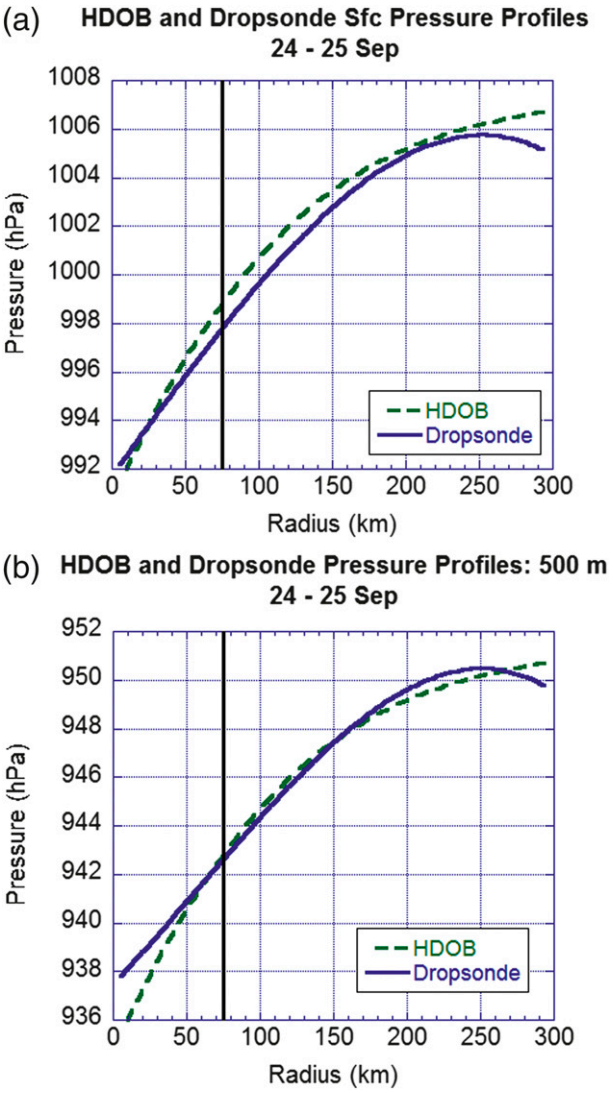

FIG. 12. Plot of radial pressure profile (hPa) estimated by a third-order polynomial curve fit of in situ dropsonde observations (solid blue line) and a third-order polynomial curve fit of HDOB extrapolated sea level pressure (dashed green line) for Tropical Storm Jangmi at the (a) surface and at (b) 500-m altitude. The solid black vertical line denotes the RMW based on the SFMR flight-level data shown previously in Fig. 6b. The HDOB extrapolated SLP was reduced using a constant offset of 55 hPa in both (a) and (b). The offset value was determined by subtracting the HDOB pressure value from the dropsonde pressure value at a radius of 75 km. This radius was chosen since it was the RMW. Note the difference in the radial pressure gradient near the RMW and that the HDOB curves have a steeper slope than the dropsonde curves, which is consistent with the findings of Bell and Montgomery (2008).

analysis using the more frequent 30-s HDOB extrapolated sea level pressure data. The error estimate was computed using the steepest pressure-gradient curve [northeast (NE) quadrant] and the flattest pressure-gradient curve [west-southwest (WSW) quadrant, hereafter

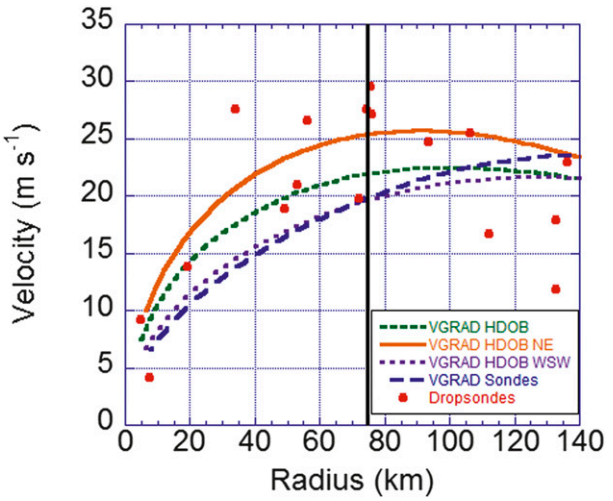

FIG. 13. Tangential wind speed ($m\,s^{-1}$) at 500-m altitude for TS Jangmi from dropsondes (solid red circles) and gradient wind speed ($m\,s^{-1}$) derived from all flight-level HDOB data (short-dashed green curve), flight-level HDOB data in NE quadrant (solid orange line), flight-level HDOB data in WSW quadrant (dotted purple line), and dropsonde data (long-dashed blue line). The solid black vertical line denotes the axisymmetric RMW based on the SFMR data. The NE and WSW quadrant curves were used to plot an upper and lower bound of the gradient wind curve, respectively. The NE quadrant contained the steepest pressure gradient, while the WSW quadrant had the flattest pressure gradient.

all quadrants are abbreviated] to compute an estimated upper and lower bound for the gradient wind curve. In this estimate, it was assumed that the radius of curvature of the tangential wind (i.e., primary circulation) was equal to the local radius. These two curves provide a reasonable uncertainty estimate of the asymmetric pressure field observed in TS Jangmi. The upper- and lower-bounding curves of the gradient wind are plotted with the HDOB and dropsonde-derived gradient wind curves and are shown in Fig. 13.

In Fig. 13, the gradient wind associated with the steepest pressure gradient curve (NE quadrant—solid orange line) still lies below five supergradient wind observations near and just within the RMW. Note also that the dropsonde curve is very similar to the gradient wind curve obtained using the flattest pressure gradient (WSW quadrant—dotted purple line). The difference between the upper and lower bound gradient wind curves is approximately $5\,m\,s^{-1}$ just outside the RMW and then around 6–7 $m\,s^{-1}$ near and just within the RMW. This difference is used to define an uncertainty estimate of $\sim\pm3\,m\,s^{-1}$ for the gradient wind curve.

From Fig. 13 we see also that the tangential wind speeds are in excess of the mean HDOB-derived gradient wind curve (dashed green line) by 5–6 $m\,s^{-1}$. The tangential winds still exceed the largest HDOB-derived

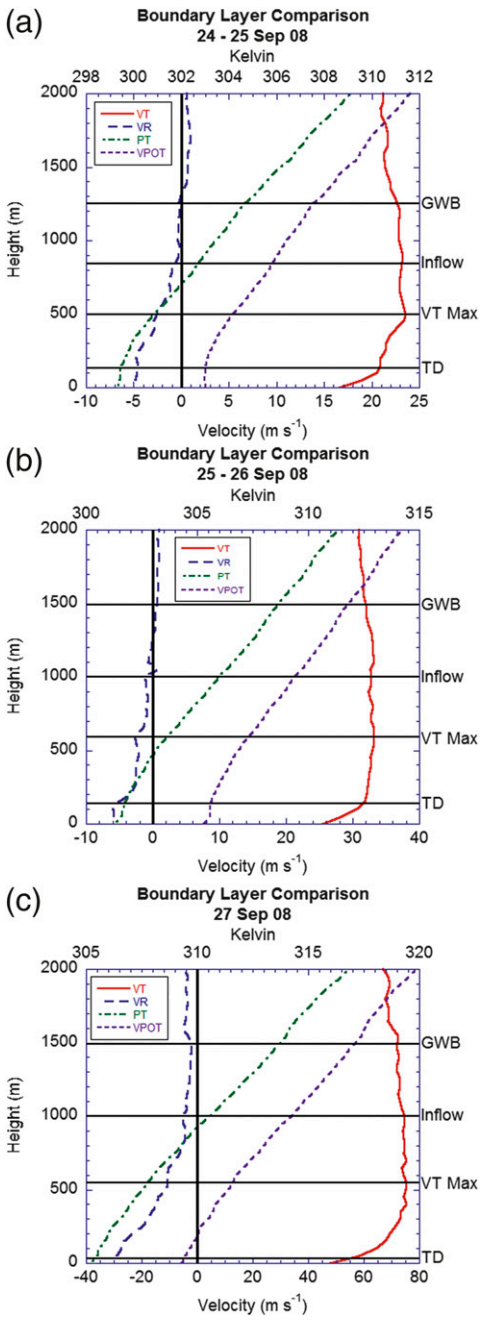

FIG. 14. Boundary layer height comparison for (a) TS Jangmi, (b) TY Jangmi, and (c) STY Jangmi using thermodynamic and dynamic definitions. Dynamic boundary layer (layer of significant gradient wind imbalance) depth depicted by solid horizontal black line labeled "GWB"; layer of significant radial inflow (≥20% of near-surface value) shown by solid horizontal black line marked "inflow"; thermodynamic boundary layer (well mixed) displayed with solid horizontal black line labeled "TD." The height of maximum tangential wind speed depicted with solid horizontal black line labeled "VT Max." Tangential wind speed composite (solid red line), radial wind speed composite (dashed blue line), potential temperature composite (dotted-dashed green line), and virtual potential temperature (small dashed purple line) are plotted on graph.

gradient wind speed curve by at least $1\,m\,s^{-1}$ after considering the estimated $\pm 3\,m\,s^{-1}$ error in the gradient wind curve and $2\,m\,s^{-1}$ RMSE for the tangential wind due to the center uncertainty.

The quadrant-by-quadrant gradient wind analysis at 500-m altitude derived from the extrapolated sea level pressure for each of the six radial legs shown in Sanger (2011, Figs. 49b,d,f,h,j,l) shows at least one observation of supergradient winds in each quadrant (ESE-1, WSW-1, SSE-1, NE-1, NW-1, and SE-2).[3] After factoring in the $\pm 3\,m\,s^{-1}$ error bar estimated from the gradient wind curve and center errors it was discovered that only 2 of the 7 supergradient wind observations were 10% or more above the gradient wind speed (11% and 19% in ESE and SE quadrants, respectively). However, 4 of the 7 observations were 9%, 8%, 6%, and 4% above the gradient wind speed in the NW, NE, WSW, and SSE quadrants, respectively. One of the data points from the SE quadrant is in gradient wind balance after taking the estimated error bar into account. Thus, 6 of the 7 supergradient wind observations based on the error bar are at least 4% above the gradient wind speed. Furthermore, these results are based on the conservative HDOB gradient wind speed estimate. If one uses the dropsonde-derived gradient wind curve, all seven of the observations are at least 10% supergradient.

e. *Boundary layer*

As discussed in Smith and Montgomery (2010), there is a plethora of definitions of the boundary layer. In their analyses of numerical simulations, Smith et al. (2009) chose to use the depth of strong inflow (radial wind speeds exceeding $2\,m\,s^{-1}$), which is reasonably well defined in their calculations. However, since the boundary layer owes its existence to the inward agradient force brought about by the reduction of the tangential wind component by surface friction, an alternative definition would be to take the depth of significant gradient wind imbalance, for example, the height at which the tangential wind is 10% greater or less than the gradient wind. We refer to this as the dynamical definition of the boundary layer. Some authors have used a thermodynamic definition of the boundary layer to characterize the depth of the mixed layer based on the virtual potential temperature structure. Since mixing in the hurricane boundary layer is primarily associated with shear-generated turbulence, we consider this definition inappropriate for application in this region. However, since

[3] For details of the error analysis, the reader is referred to Sanger (2011, chapter 4, section 3d).

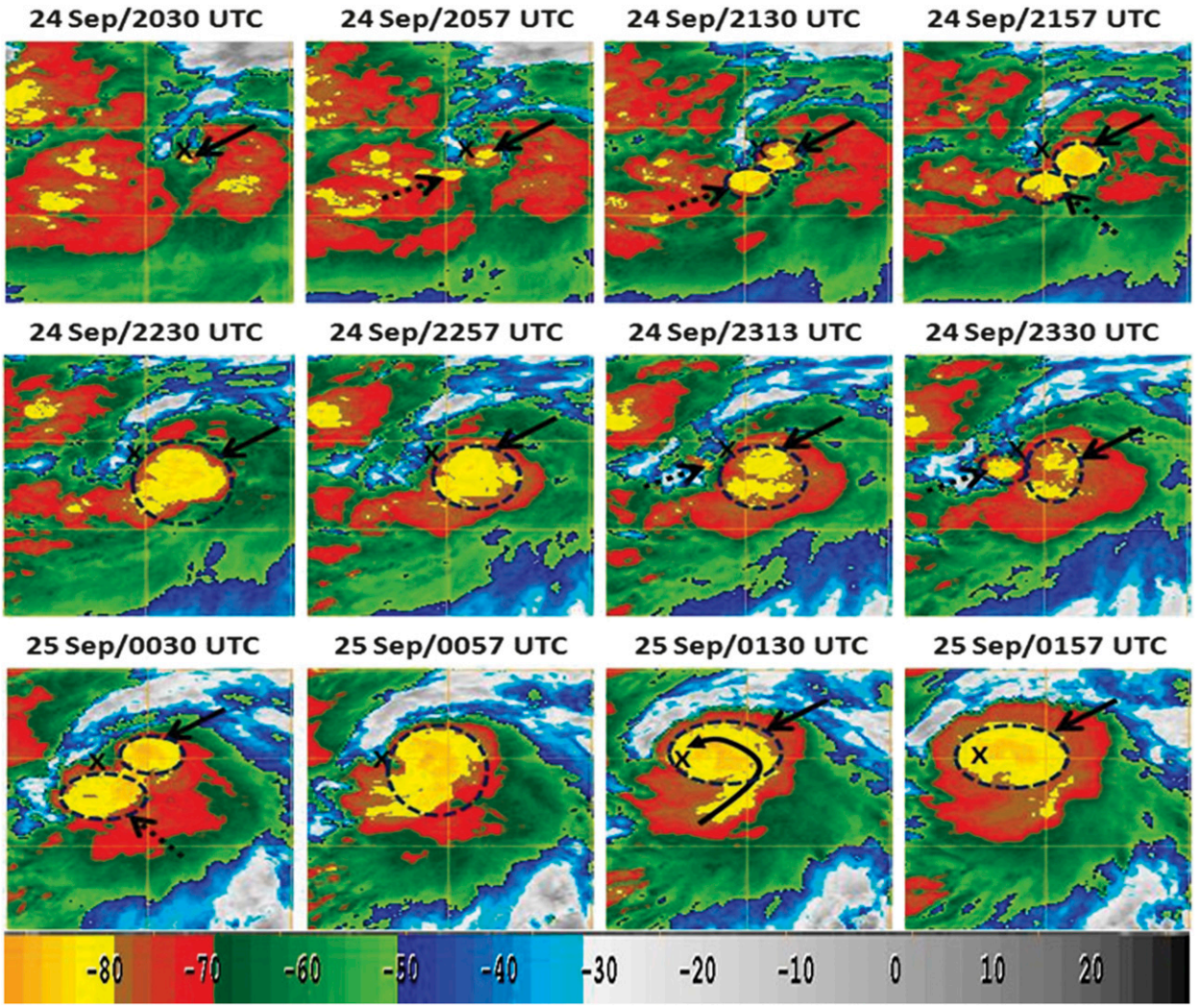

FIG. 15. Series of 1-km MTSAT infrared imagery of deep convective clouds in TS Jangmi from 2030 UTC 24 Sep to 0157 UTC 25 Sep 2008. Dashed blue circles indicate deep convection and its approximate areal extent and shape. TS Jangmi center based on the 10-min storm track file (see section 3e for description) is shown with black "×." Note the increase in horizontal coverage in both areas of deep convective clouds, possible cloud merger in 0057 UTC 25 Sep panel, and inward spiral of clouds in second to last panel at 0130 UTC 25 Sep. The color bar at the bottom of the plot associates cloud-top temperatures with various colors. The coldest cloud-top temperatures are shown with shades of red and yellow (from −70° to −90°C). (Imagery courtesy of Naval Research Laboratory, Monterey, CA.)

the data are available we show the depth of this layer for comparison.

Figure 14 shows the composite wind and thermal structure of the dynamic boundary layer during the evolution of Jangmi. In the figure, VT and VR denote the tangential and radial components of storm-relative wind, respectively, VPOT denotes the virtual potential temperature, and PT denotes the potential temperature. The depth of significant low-level radial inflow (VR ≥ 20% of its near-surface value) is shown with the solid black horizontal line labeled "inflow." The height of the peak tangential wind speed is depicted with a solid black horizontal line labeled "VT MAX." The estimated dynamic boundary layer depth is denoted by the solid black horizontal line labeled "GWB." The thermodynamic boundary layer depth is depicted by the solid black horizontal line labeled "TD."

These data indicate that the dynamical boundary layer is much deeper than the well-mixed layer, consistent with the findings of Zhang et al. (2009) and Zhang et al. (2011). Of particular significance, the average maximum tangential wind component lies well within the dynamical boundary layer and within the layer of significant radial inflow on all three days.

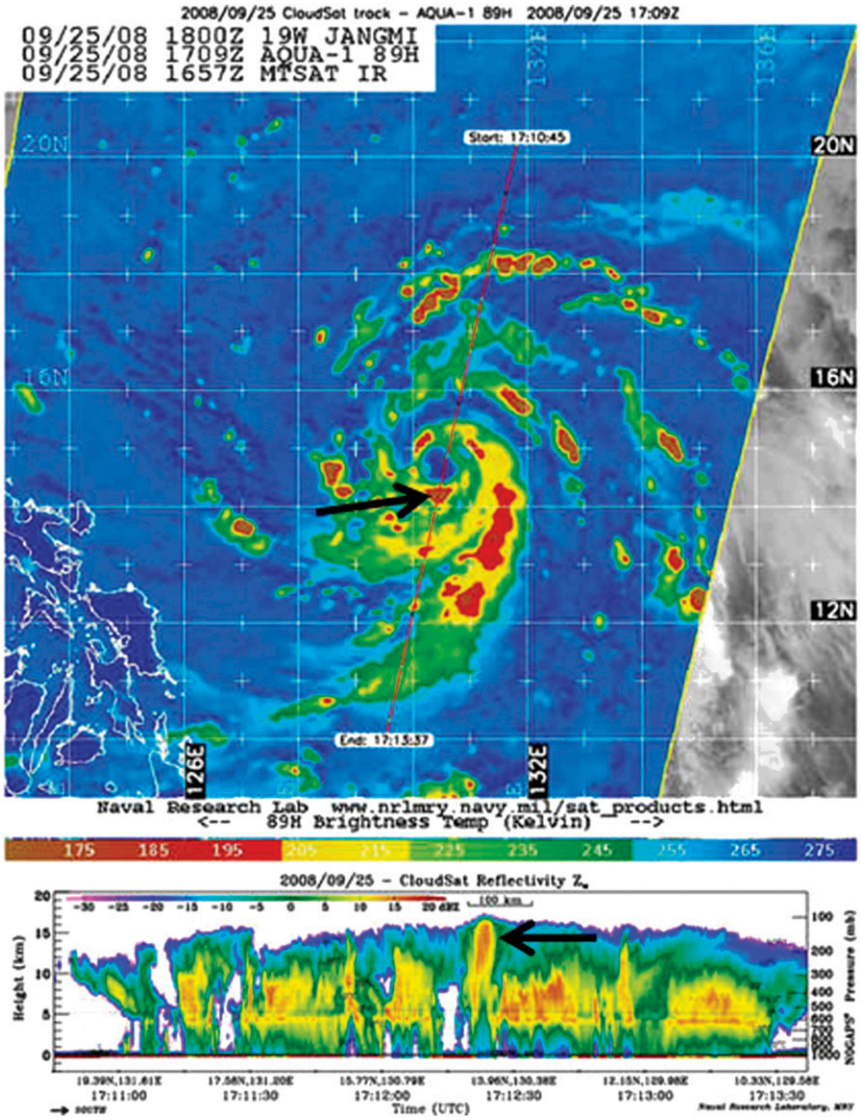

FIG. 16. (bottom) *CloudSat* reflectivity through Typhoon Jangmi during pass from north to south from 1711 to 1713 UTC 25 Sep 2008 with (top) associated *Aqua* microwave satellite image at 1709 UTC 25 Sep 2008. Black arrows depict the deep convection in the southern eyewall extending up to 17-km altitude. The color bar in between the reflectivity and satellite image associates cloud-top temperatures (K) with various colors. The coldest cloud-top temperatures are shown with shades of red and orange (200–170 K). (Images courtesy of Colorado State University/NESDIS/CIRA, Fort Collins, CO.)

5. An asymmetric view of Jangmi's spinup

a. Background

Numerical modeling studies by Montgomery et al. (2006a), Wissmeier and Smith (2011), and Kilroy and Smith (2013) have shown that the stretching of vertical vorticity by growing convection amplifies this vorticity component by more than an order of magnitude to produce a local vorticity maximum and that the amplified vorticity remains for a long time after the initial updraft has decayed. The predicted vorticity levels are comparable with those observed in recent research on tropical depressions (Houze et al. 2009; Bell and Montgomery 2010; Raymond and López-Carrillo 2011). One of the main findings in Wissmeier and Smith (2011) was that significant amplification of the vertical vorticity occurs even for a background rotation rate typical of the undisturbed tropical atmosphere and for clouds of only moderate vertical extent such as cumulus congestus clouds. Thus, one should focus not only on the deepest

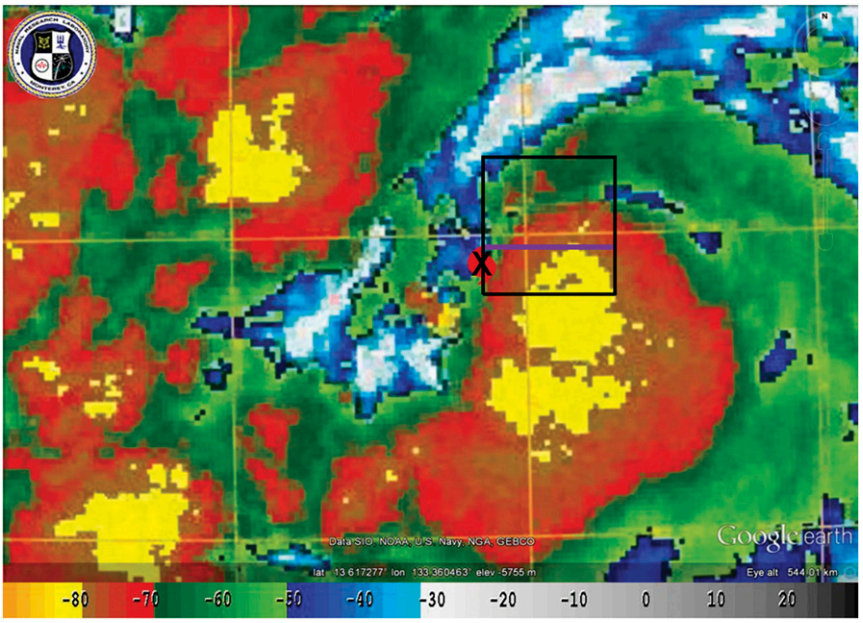

FIG. 17. 1-km MTSAT infrared imagery at 2313 UTC 24 Sep 2008 during NRL P-3 ELDORA mission into Tropical Storm Jangmi. The ELDORA data domain is shown with the black rectangle. The 0000 UTC 25 Sep storm position based on the 10-min storm track file is shown with black "×" in bottom-left portion of domain. The location of the vertical cross section shown later in Fig. 20 is depicted by the solid purple line. The color bar at the bottom of the image associates cloud-top temperatures with various colors. The coldest cloud-top temperatures are shown with shades of red and yellow (from −70° to −90°C).

convection, but consider also the net effect of the moderate convection in the aggregate.

Deep convective cells of varying intensity were observed during the spinup of Jangmi. A brief investigation of this convective activity is presented first to provide a context for a quantitative assessment of the vorticity and convergence in some of the updrafts in TS Jangmi, using results from the ELDORA mesoscale analysis of cells that were underneath cold cloud-top temperatures of ≤−65°C.

b. *Analysis of convection*

The evolution of convective cells during the spinup of Jangmi is shown using satellite imagery in Fig. 15 during the tropical storm stage. Between 2030 UTC 24 September and 0257 UTC 25 September, two major convective bursts commenced at 2030 UTC 24 September (panels 1–7 in Fig. 15) and 2330 UTC 24 September (panels 8–12 in Fig. 15). These bursts consisted of the development of cells and their associated anvil clouds near the center of TS Jangmi with extremely cold cloud-top temperatures of <−85°C. Throughout this period, the anvil clouds grew in size and merged into one large region of extremely cold cloud tops covering an area of around 46 000 km^2. A variety of additional observational sources indicated evidence of other convective burst activity during the 3-day spinup period. For example, a timely *CloudSat* pass at 1709 UTC 25 September sampled a deep convective cell in the storm's southern quadrant located near the center of the storm that extended to an altitude of nearly 17 km (Fig. 16). Other areas of both moderate and deep convection were observed in the northern and southern quadrants of Jangmi.

c. *ELDORA radar observations in Tropical Storm Jangmi*

The ELDORA radar on board the NRL P-3 observed some of the deep convection in TS Jangmi on 24 September 2008. There were many instances where the radar sampled enhanced levels of vertical vorticity within convective clouds. As an illustration, we show an example of a convective complex with a well-defined vertical vorticity signature. The ELDORA domain for the period 2310–2320 UTC 24 September is overlaid with the Multifunctional Transport Satellites (MTSAT) infrared imagery on 2313 UTC 24 September, which shows extremely cold cloud-top temperatures of <−75°C (Fig. 17). The motivation for this radar analysis is to

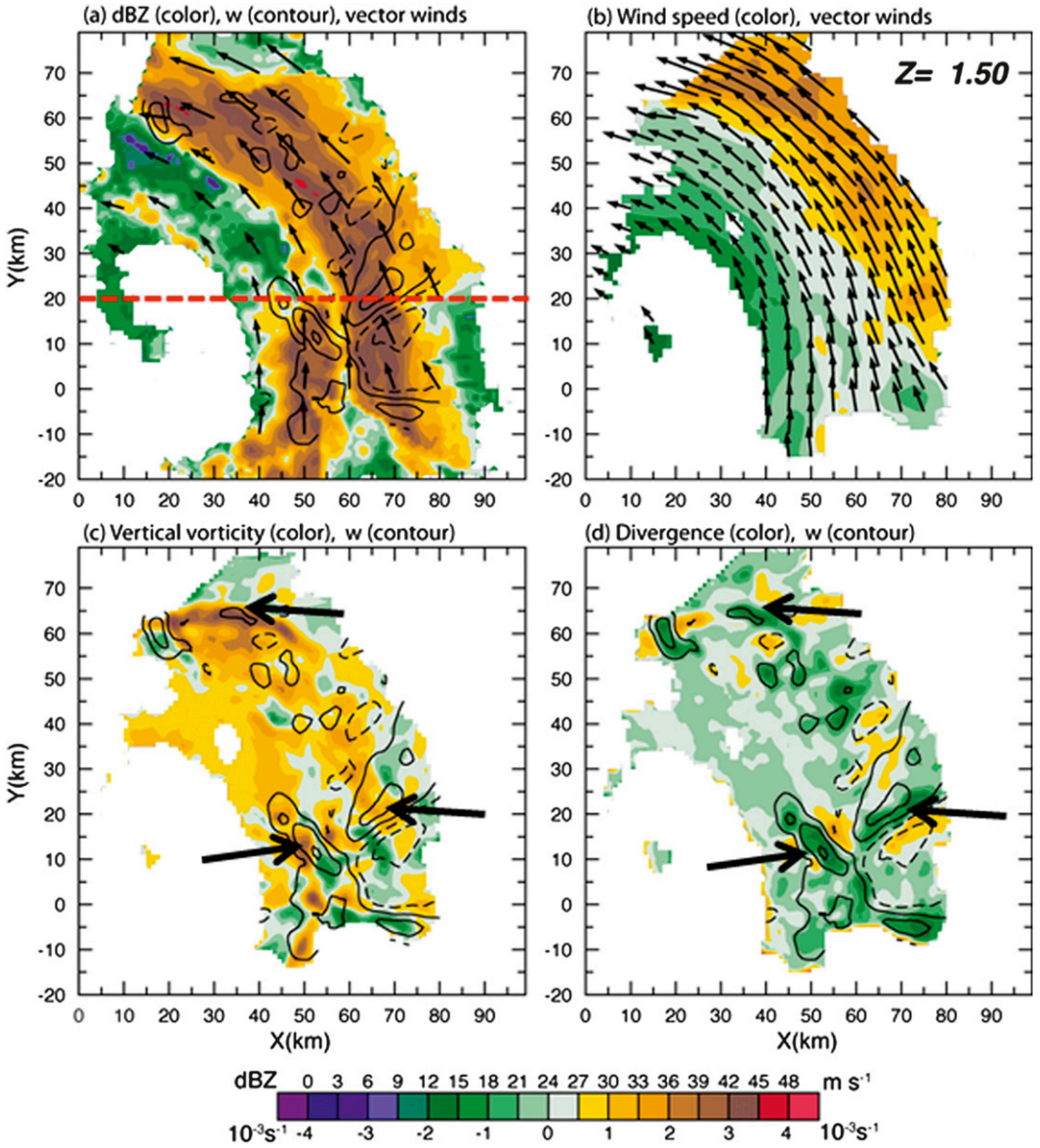

FIG. 18. ELDORA analysis from 2310 to 2320 UTC 24 Sep 2008. (a) Horizontal plan view of radar reflectivity (color, dBZ), wind vectors, and vertical velocity (contour, 2 m s^{-1} increments; solid contours are positive) at 1.5-km altitude. The red dashed line indicates location of the vertical slice to be examined later in Fig. 20. (b) Wind vectors and speed (color contoured, m s^{-1}) in the Earth-relative frame at 1.5-km altitude. (c) Horizontal plan view of relative vertical vorticity (color, 10^{-3} s^{-1}) and vertical velocity (contour, 2 m s^{-1} increments; solid contours are positive) at 1.5-km altitude. (d) Divergence (color, 10^{-3} s^{-1}) and vertical velocity (contour, 2 m s^{-1} increments; solid contours are positive) at 1.5-km altitude. Arrows show regions of cyclonic vorticity, convergence, and updrafts.

determine whether the convection located underneath the cold infrared imagery cloud tops of TS Jangmi during 2310–2320 UTC 24 September has rotation.

The analysis of the 1.5-km altitude radar data displayed in Fig. 18a reveals convection arrayed in spiral bands around the storm center. Earth-relative winds in Fig. 18b indicate strong southerly to southeasterly flow of 35–40 m s^{-1} located in the outermost spiral band. The innermost spiral band has lower wind speeds between 12 and 27 m s^{-1}. The vertical vorticity and vertical velocity in Fig. 18c reveal three updraft regions collocated with regions of elevated relative vorticity in the ELDORA domain. In these regions, large relative vorticity on the order of 2×10^{-3} s^{-1} and vertical velocities between 4 and 5 m s^{-1} are analyzed. All three of these regions are in areas of significant low-level convergence also, with values on the order of 2×10^{-3} s^{-1} (Fig. 18d). A few other areas of enhanced relative vorticity, convergence,

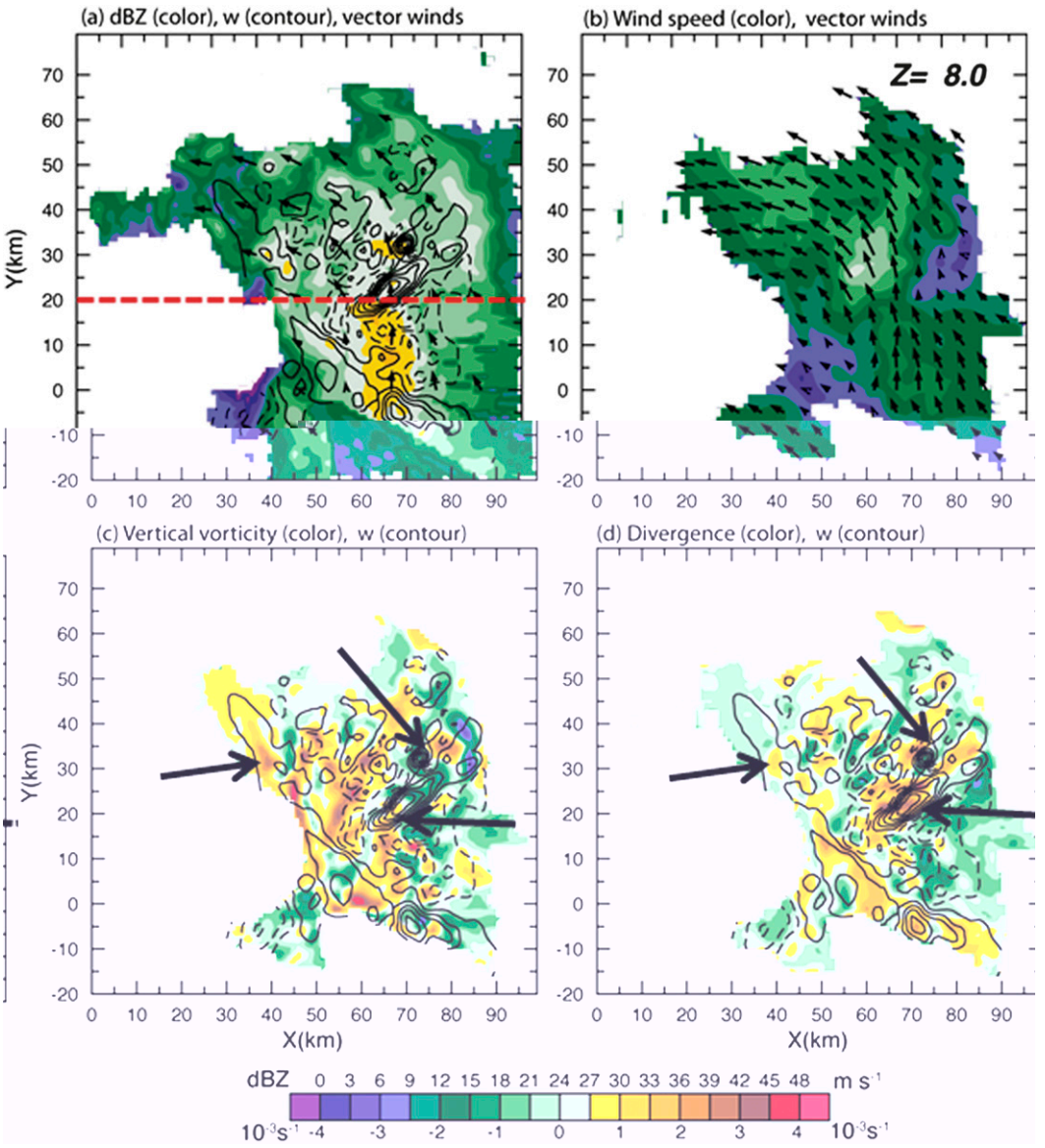

FIG. 19. ELDORA analysis from 2310 to 2320 UTC 24 Sep 2008. (a) Horizontal plan view of radar reflectivity (color, dBZ), wind vectors, and vertical velocity (contour, 2 m s^{-1} increments; solid contours are positive) at 8-km altitude. The red dashed line indicates location of the vertical slice to be examined later in Fig. 20. (b) Wind vectors and speed (color contoured, m s^{-1}) in the Earth-relative frame at 8.0-km altitude. (c) Horizontal plan view of relative vertical vorticity (color, 10^{-3} s^{-1}) and vertical velocity (contour, 2 m s^{-1} increments; solid contours are positive) at 8.0-km altitude. (d) Divergence (color, 10^{-3} s^{-1}) and vertical velocity (contour, 2 m s^{-1} increments; solid contours are positive) at 8-km altitude. Arrows show regions of cyclonic vorticity, divergence, and updrafts.

and vertical velocity with values on the order of 2×10^{-3} s^{-1}, 2×10^{-3} s^{-1}, and 2 m s^{-1}, respectively, are found in the northern half of the outer spiral band.

In the outermost spiral band in Figs. 18c,d, there are multiple updraft and downdraft dipoles, as well as positive and negative relative vorticity dipoles. The most dominate dipole pattern is observed in the lower right portion of Figs. 18c,d. In contrast, the innermost spiral band contains several areas having updrafts collocated with elevated positive relative vorticity.

The analysis of the 8.0-km altitude ELDORA radar data in Fig. 19a reveals reflectivity values from 18 dBZ to around 30 dBZ at and south of $y = 20$ km and between $x = 63$ and $x = 75$ km. Earth-relative winds in Fig. 19b indicate a southerly to southeasterly flow of 21–27 m s^{-1} in the outermost spiral band. The innermost spiral band

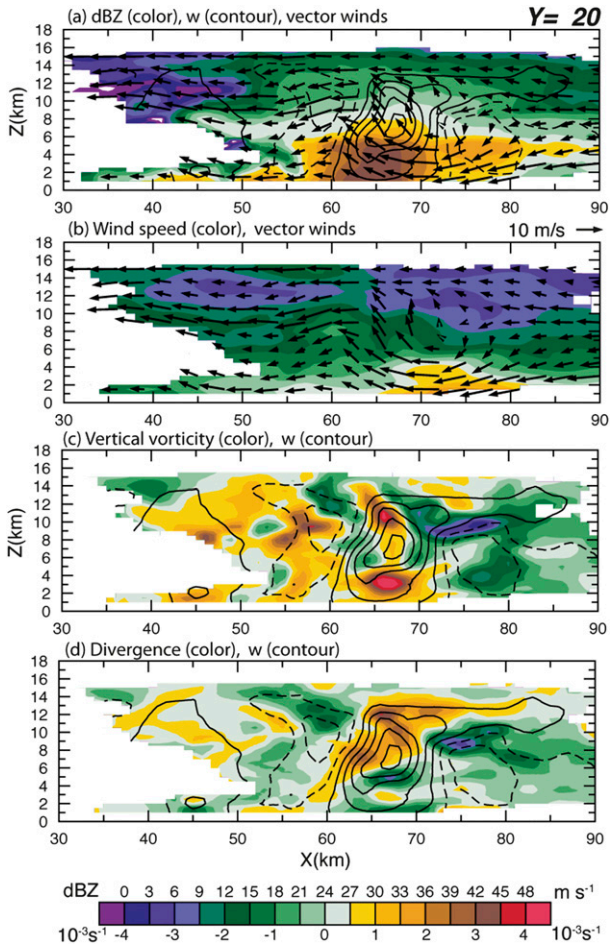

FIG. 20. ELDORA vertical-zonal cross-sectional analysis from 2310 to 2320 UTC 24 Sep 2008. (a) Reflectivity (color), wind vectors in the vertical-zonal plane, and vertical velocity (contours, $2\,m\,s^{-1}$ increments; solid contours are positive). (b) Earth-relative wind velocity (color, $m\,s^{-1}$), and wind vectors in the x–z plane. (c) Vertical relative vorticity (color) and vertical velocity (contours, $m\,s^{-1}$ in $2\,m\,s^{-1}$ increments; solid contours are positive). (d) Divergence (color, $10^{-3}\,s^{-1}$) and vertical velocity (contour, $2\,m\,s^{-1}$ increments).

contains lower wind speeds between 2 and $15\,m\,s^{-1}$. Near the center of the outermost spiral band, enhanced vertical vorticity values of $2 \times 10^{-3}\,s^{-1}$ are collocated with strong updraft velocities of over $9\,m\,s^{-1}$ and divergence values of about $3 \times 10^{-3}\,s^{-1}$ (Figs. 19c,d). There is a smaller region also of elevated levels of collocated positive relative vorticity on the order of $1 \times 10^{-3}\,s^{-1}$ and vertical velocities of 1–3 $m\,s^{-1}$.

The ELDORA radar analysis at both 1.5- and 8.0-km altitude shows that underneath a region of extremely cold infrared cloud tops there are multiple rotating convective cells. To investigate further the presence of rotating convection, a vertical cross section of the strongest updraft is taken at $y = 20$ km (denoted by the dashed red line in Figs. 18a and 19a).

The vertical cross section in Fig. 20a reveals the existence of strong, upright convection with greater than 40-dBZ reflectivity values extending to an altitude of around 6 km with a horizontal extent of about 12 km and echo tops stretching up to an altitude of more than 15 km. Strong updraft velocities on the order of 4–9 $m\,s^{-1}$ are analyzed in the moderate to strong radar reflectivities extending to around 11-km altitude.

In Fig. 20c, an area of enhanced vertical vorticity is collocated with a 12-km-wide vertical updraft from an altitude of 1.5 up to 13 km. Two relative vorticity peaks of greater than $4 \times 10^{-3}\,s^{-1}$ at heights of 3 and 11 km are collocated with ~3–4 $m\,s^{-1}$ vertical velocities. The stretching of ambient vorticity is a most likely source of the low-level peak relative vorticity. However, both tilting and advection processes may be playing a role in creating the relative vorticity maximum observed at the upper levels. There is a maximum vertical velocity of $9\,m\,s^{-1}$ in between the two vertical vorticity peaks at an altitude of 8 km. This velocity maximum is collocated with vertical relative vorticity of approximately $0.5 \times 10^{-3}\,s^{-1}$. In Fig. 20d, large horizontal values of divergence between -2×10^{-3} and $-3.5 \times 10^{-3}\,s^{-1}$ are observed below 2-km altitude and between 4- and 6-km altitude.

The findings here are consistent with those obtained in previous studies of convective-scale asymmetric features of tropical cyclones using airborne Doppler radar and dropsonde data (Marks and Houze 1984; Reasor et al. 2005; Reasor et al. 2009; Houze et al. 2009; Bell and Montgomery 2010; Raymond and López-Carrillo 2011). The observed occurrence of vortical convection is consistent also with recent numerical modeling studies of Hendricks et al. (2004), Montgomery et al. (2006a), Nguyen et al. (2008), Shin and Smith (2008), and Fang and Zhang (2011), which suggested the importance of vortical convection to spinup of the inner core. However, since there was a limited amount of data analyzed in this case, further studies of storms using ELDORA radar are necessary to yield a more rigorous assessment of rotating convection and to quantify its impact on tropical cyclone spinup.

6. Summary and conclusions

An observational study of the spinup of Supertyphoon Jangmi was carried out using data collected during the TCS-08 field experiment. These data include GPS dropsondes, ELDORA radar, and satellite imagery. Individual and composite vertical profiles of the dropsonde data were examined to determine the structure of

the inner-core boundary layer of the intensifying storm. It was shown that the azimuthally averaged maximum tangential wind speed lies well within the dynamical boundary layer on all three days.

An analysis of gradient wind balance was obtained at selected heights up to 1500 m from the dropsonde and HDOB data. The results suggest the presence of significant supergradient winds within the dynamic boundary layer and near the RMW in all three stages of the storm evolution. The largest supergradient wind speeds occurred near and just inside the RMW during the supertyphoon stage of Jangmi, but the highest supergradient winds relative to the local gradient wind occurred in the TS phase. The evidence suggesting the existence and spatial structure of supergradient winds near and within the RMW supports the arguments presented by Smith et al. (2008), Smith et al. (2009), and Smith and Montgomery (2010) that unbalanced boundary layer dynamics in the inner-core region are an important component in determining the maximum axisymmetric-mean radial and tangential flow at all times during the evolution of the storm.

Fluid dynamical reasoning suggests convection in a rotating environment should be vortical in nature. This expectation is confirmed by the ELDORA radar analysis, which showed multiple areas of rotating updrafts in the inner-core circulation some hours before its intensification to a typhoon. In one instance, there was a region of enhanced cyclonic vorticity on the order of $2 \times 10^{-3}\,\mathrm{s}^{-1}$ collocated with a 12-km-wide updraft, which contained average velocities of around 4–5 $\mathrm{m\,s}^{-1}$ and a peak of 9 $\mathrm{m\,s}^{-1}$ at 8-km altitude. This region had also strong low-level and midlevel convergence. This region was collocated with cold cloud-top temperatures as shown in the infrared satellite imagery. Various satellite images covering the entire 3-day spinup period showed bursts of deep convection with cold cloud-top temperatures, suggesting that rotating convection was prevalent during the entire spinup of Jangmi. The findings are consistent with those of previous studies examining convective-scale features of tropical cyclones using airborne Doppler radar.

The foregoing results support the hypothesis that rotating convection and the accompanying system-scale spinup mechanisms described herein, contributed to the intensification of Tropical Cyclone Jangmi. Of course, this is only one storm and clearly further studies of storms using Doppler radar are required to provide a more complete sample of vortical convective structures and to quantify their effect on the primary circulation.

In view of the caveats involved with the axisymmetric gradient wind calculations, future research aircraft penetrations should aim to release dropsondes more frequently across the RMW during each radial leg to allow improved resolution of the radial pressure gradient there and permit an assessment of whether supergradient winds exist in the dynamic boundary layer at the tropical storm stage more generally. As a first step in this direction, such an analysis is being conducted for the spinup portion of Tropical Storm Earl, which rapidly intensified to a major hurricane during a recent 2010 field experiment. The results of this analysis will be reported in due course.

Acknowledgments. We are grateful to the U.S. Naval Postgraduate School, the Office of Naval Research (Grant N001408WR20129), and the National Science Foundation for sponsoring the TCS08/TPARC field experiment, supporting our participation in the experiment, and facilitating our analysis of the data. We thank Peter Black at the Naval Research Laboratory in Monterey and Russ Elsberry, Frank Giraldo, and Pat Harr at Naval Postgraduate School for their helpful comments. We express our gratitude also to NOAA/HRD for providing the Willoughby and Chelmow (1982) derived storm centers for Jangmi. We extend our appreciation to NCAR/EOL for providing the quality controlled dropsonde and NRL P-3 flight-level data for analysis. Last, we would like to offer our sincere thanks to the brave NRL P-3 and WC-130J "Hurricane Hunter" aircrews that courageously flew into these tropical tempests to collect data so that we may better understand the spinup process.

REFERENCES

Bell, M. M., and M. T. Montgomery, 2008: Observed structure, evolution, and potential intensity of category 5 Hurricane Isabel (2003) from 12 to 14 September. *Mon. Wea. Rev.,* **136,** 2023–2046.

——, and ——, 2010: Sheared deep vortical convection in pre-depression Hagupit during TCS08. *Geophys. Res. Lett.,* **37,** L06802, doi:10.1029/2009GL042313.

——, ——, and W.-C. Lee, 2012: An axisymmetric view of concentric eyewall evolution in Hurricane Rita (2005). *J. Atmos. Sci.,* **69,** 2414–2432.

Bui, H. H., R. K. Smith, M. T. Montgomery, and J. Peng, 2009: Balanced and unbalanced aspects of tropical cyclone intensification. *Quart. J. Roy. Meteor. Soc.,* **135,** 1715–1731.

Carrier, G. F., 1971: The intensification of hurricanes. *J. Fluid Mech.,* **49,** 145–148.

Charney, J. G., and A. Eliassen, 1964: On the growth of the Hurricane Depression. *J. Atmos. Sci.,* **21,** 68–75.

Chu, J. H., A. Levine, S. Daida, D. Schiber, E. Fukada, and C. R. Sampson, cited 2009: JTWC western North Pacific best track data. [Available online at http://www.usno.navy.mil/NOOC/nmfc-ph/RSS/jtwc/best_tracks/2008/2008s-bwp/bwp192008.txt.]

Cooper, G. A., and R. J. Falvey, 2009: U.S. Naval Maritime Forecast Center/Joint Typhoon Warning Center 2008 Annual

Tropical Cyclone Report. 116 pp. [Available online at http://www.usno.navy.mil/NOOC/nmfc-ph/RSS/jtwc/atcr/2008atcr.pdf.]

Elsberry, R. L., and P. A. Harr, 2008: Tropical cyclone structure (TCS08) field experiment: Science basis, observational platforms, and strategy. *Asia-Pac. J. Atmos. Sci.,* **44,** 209–231.

Emanuel, K. A., 1989: The finite-amplitude nature of tropical cyclogenesis. *J. Atmos. Sci.,* **46,** 3431–3456.

——, 1997: Some aspects of hurricane inner-core dynamics and energetics. *J. Atmos. Sci.,* **54,** 1014–1026.

——, 2003: Tropical cyclones. *Annu. Rev. Earth Planet. Sci.,* **31,** 75–104, doi:10.1146/annurev.earth.31.100901.141259.

——, J. D. Neelin, and C. S. Bretherton, 1994: On large-scale circulations in convecting atmospheres. *Quart. J. Roy. Meteor. Soc.,* **120,** 1111–1143.

Fang, J., and F. Zhang, 2011: Evolution of multiscale vortices in the development of Hurricane Dolly (2008). *J. Atmos. Sci.,* **68,** 103–122.

Franklin, J. L., M. L. Black, and K. Valde, 2003: GPS dropwindsonde wind profiles in hurricanes and their operational implications. *Wea. Forecasting,* **18,** 32–44.

Giammanco, I. M., J. L. Schroeder, M. D. Powell, and D. A. Smith, 2008: GPS dropwindsonde observations of tropical cyclone low-level wind maxima. Preprints, *28th Conf. on Hurricanes and Tropical Meteorology,* Orlando, FL, Amer. Meteor. Soc., P2E.1. [Available online at https://ams.confex.com/ams/pdfpapers/137230.pdf.]

Hendricks, E. A., M. T. Montgomery, and C. A. Davis, 2004: The role of ''vertical'' hot towers in the formation of Tropical Cyclone Diana (1984). *J. Atmos. Sci.,* **61,** 1209–1232.

Hildebrand, P. H., and Coauthors, 1996: The ELDORA/ASTRAIA airborne Doppler weather radar: High-resolution observations from TOGA COARE. *Bull. Amer. Meteor. Soc.,* **77,** 213–232.

Hock, T. F., and J. L. Franklin, 1999: The NCAR GPS dropwindsonde. *Bull. Amer. Meteor. Soc.,* **80,** 407–420.

Holton, J. R., 2004: *An Introduction to Dynamic Meteorology.* 4th ed. Academic Press, 535 pp.

Houze, R. A., Jr., W. C. Lee, and M. M. Bell, 2009: Convective contribution to the genesis of Hurricane Ophelia (2005). *Mon. Wea. Rev.,* **137,** 2778–2800.

Kaplan, J., and M. DeMaria, 2003: Large-scale characteristics of rapidly intensifying tropical cyclones in the North Atlantic basin. *Wea. Forecasting,* **18,** 1093–1108.

Kepert, J., 2001: The dynamics of boundary layer jets within the tropical cyclone core. Part I: Linear theory. *J. Atmos. Sci.,* **58,** 2469–2484.

——, and Y. Wang, 2001: The dynamics of boundary layer jets within the tropical cyclone core. Part II: Nonlinear enhancement. *J. Atmos. Sci.,* **58,** 2485–2501.

Kilroy, G., and R. K. Smith, 2013: A numerical study of rotating convection during tropical cyclogenesis. *Quart. J. Roy. Meteor. Soc.,* **139,** 1255–1269, doi:10.1002/qj.2022.

Marks, F. D., Jr., and R. A. Houze Jr., 1984: Airborne Doppler radar observations in Hurricane Debby. *Bull. Amer. Meteor. Soc.,* **65,** 569–582.

Montgomery, M. T., and R. K. Smith, 2013: Paradigms for tropical cyclone intensification. *Aust. Meteor. Ocean. J.* (Bruce Morton Memorial Volume), in press.

——, M. E. Nicholls, T. A. Cram, and A. B. Saunders, 2006a: A vortical hot tower route to tropical cyclogenesis. *J. Atmos. Sci.,* **63,** 355–386.

——, M. M. Bell, S. D. Aberson, and M. L. Black, 2006b: Hurricane Isabel (2003): New insights into the physics of intense storms. Part I: Mean vortex structure and maximum intensity estimates. *Bull. Amer. Meteor. Soc.,* **87,** 1335–1347.

——, S. V. Nguyen, R. K. Smith, and J. Persing, 2009: Is WISHE essential for tropical cyclone intensification? *Quart. J. Roy. Meteor. Soc.,* **135,** 1697–1714.

Nguyen, S. V., R. K. Smith, and M. T. Montgomery, 2008: Tropical cyclone intensification and predictability in three dimensions. *Quart. J. Roy. Meteor. Soc.,* **134,** 563–582.

Ooyama, K. V., 1969: Numerical simulation of the life cycle of tropical cyclones. *J. Atmos. Sci.,* **26,** 3–40.

Parsons, D., P. A. Harr, T. Nakazawa, S. Jones, and M. Weissmann, 2008: An overview of the THORPEX-Pacific Asian Regional Campaign (T-PARC) during August-September 2008. Preprints, *28th Conf. on Hurricanes and Tropical Meteorology,* Orlando, FL, Amer. Meteor. Soc., 7C.7. [Available online at https://ams.confex.com/ams/28Hurricanes/techprogram/paper_138431.htm.]

Persing, J., M. T. Montgomery, J. McWilliams, and R. K. Smith, 2013: Asymmetric and axisymmetric dynamics of tropical cyclones. *Atmos. Chem. Phys.,* in press.

Powell, M. D., P. J. Vickery, and T. A. Reinhold, 2003: Reduced drag coefficient for high wind speeds in tropical cyclones. *Nature,* **422,** 279–283.

Raymond, D. J., and C. López-Carrillo, 2011: The vorticity budget of developing Typhoon Nuri (2008). *Atmos. Chem. Phys.,* **11,** 147–163.

Reasor, P. D., M. T. Montgomery, and L. F. Bosart, 2005: Mesoscale observations of the genesis of Hurricane Dolly (1996). *J. Atmos. Sci.,* **62,** 3151–3171.

——, M. D. Eastin, and J. F. Gamache, 2009: Rapidly intensifying Hurricane Guillermo (1997). Part I: Low-wavenumber structure and evolution. *Mon. Wea. Rev.,* **137,** 603–631.

Rogers, R., and Coauthors, 2006: The Intensity Forecasting Experiment: A NOAA multiyear field program for improving tropical cyclone intensity forecasts. *Bull. Amer. Meteor. Soc.,* **87,** 1523–1537.

Rotunno, R. R., and K. A. Emanuel, 1987: An air–sea interaction theory for tropical cyclones. Part II: Evolutionary study using a nonhydrostatic axisymmetric numerical model. *J. Atmos. Sci.,* **44,** 542–561.

Sanger, N. T., cited 2008a: USAF C-130 scientist mission summary report (T-PARC_2008). Tropical Storm Jangmi from 24–25 September 2008, Rep. AF306 0247W Jangmi. [Available online at http://catalog.eol.ucar.edu/cgi-bin/tparc_2008/htmlwrap?file_url=/tparc_2008/report/usaf_c130/20080924/report.usaf_c130.200809241713.mission_summary.html.]

——, cited 2008b: USAF C-130 scientist mission summary report (T-PARC_2008). Supertyphoon Jangmi from 27 September 2008, Rep. AF306 0747W Jangmi. [Available online at http://catalog.eol.ucar.edu/cgi-bin/tparc_2008/htmlwrap?file_url=/tparc_2008/report/usaf_c130/20080927/report.usaf_c130.200809270208.mission_summary.html.]

——, 2011: An observational study of tropical cyclone spin-up in Supertyphoon Jangmi and Hurricane Georges. Ph.D. dissertation, Dept. of Meteorology, Naval Postgraduate School, 187 pp.

Shin, S., and R. K. Smith, 2008: Tropical cyclone intensification and predictability in a minimal three dimensional model. *Quart. J. Roy. Meteor. Soc.,* **134,** 1661–1671.

Smith, R. K., and M. T. Montgomery, 2010: Hurricane boundary layer theory. *Quart. J. Roy. Meteor. Soc.,* **136,** 1665–1670.

——, and G. L. Thomsen, 2010: Dependence of tropical cyclone intensification on the boundary layer representation in a numerical model. *Quart. J. Roy. Meteor. Soc.,* **136,** 1671–1685.

——, M. T. Montgomery, and S. Vogl, 2008: A critique of Emanuel's hurricane model and potential intensity theory. *Quart. J. Roy. Meteor. Soc.,* **134,** 551–561.

——, ——, and S. V. Nguyen, 2009: Tropical cyclone spin-up revisited. *Quart. J. Roy. Meteor. Soc.,* **135,** 1321–1335.

Testud, J., P. H. Hildebrand, and W. C. Lee, 1995: A procedure to correct airborne Doppler radar data for navigation errors using the echo returned from the earth's surface. *J. Atmos. Oceanic Technol.,* **12,** 800–820.

Uhlhorn, E. W., P. G. Black, J. L. Franklin, M. Goodberlet, J. Carswell, and A. S. Goldstein, 2007: Hurricane surface wind measurements from an operational stepped frequency microwave radiometer. *Mon. Wea. Rev.,* **135,** 3070–3085.

Williamson, S. P., and Coauthors, 2009: Office of Federal Coordinator for Meteorological services and supporting research (OFCM) national hurricane operations plan. FCM-P12-2009, 160 pp.

Willoughby, H. E., 1990: Gradient balance in tropical cyclones. *J. Atmos. Sci.,* **47,** 265–274.

——, and M. B. Chelmow, 1982: Objective determination of hurricane tracks from aircraft observations. *Mon. Wea. Rev*., **110,** 1298–1305.

Wissmeier, U., and R. K. Smith, 2011: Tropical cyclone convection: The effects of ambient vertical vorticity. *Quart. J. Roy. Meteor. Soc.,* **137,** 845–857.

Zhang, D., Y. Liu, and M. K. Yau, 2001: A multiscale numerical study of Hurricane Andrew (1992). Part IV: Unbalanced flows. *Mon. Wea. Rev.,* **129,** 92–107.

Zhang, J. A., W. M. Drennan, P. G. Black, and J. R. French, 2009: Turbulence structure of the hurricane boundary layer between the outer rainbands. *J. Atmos. Sci.,* **66,** 2455–2467.

——, R. F. Rogers, D. S. Nolan, and F. D. Marks, 2011: On the characteristic height scales of the hurricane boundary layer. *Mon. Wea. Rev.,* **139,** 2523–2535.